Optimisation studies for the pion-induced Drell-Yan measurement at the AMBER experiment

Rita de Sousa Ataíde da Silva

Thesis to obtain the Master of Science Degree in

Engineering Physics

Supervisors: Dr. Catarina Marques Quintans
Prof. Pedro Morais Salgueiro Teixeira de Abreu

Examination Committee

Chairperson: Prof. Mário João Martins Pimenta
Supervisor: Prof. Pedro Morais Salgueiro Teixeira de Abreu
Member of the Committee: Prof. Rute Costa Batalha Pedro
Prof. Carlos Davide da Rocha Azevedo

November 2022

Acknowledgements

First, I would like to thank my supervisor Catarina Quintans for all the guidance and continuos support. During this project I have learned a lot and trully appreciate your patience and help during the writing process. I would also like to thank her for the opportunity to participate in the project "CERN/FISPAR/0016/2021", and FCT for the financial support. In the scope of the project, I was given the opportunity to go to CERN, to visit the experimental hall of COMPASS (in the future it will be AMBER's) and to meet the researchers in the collaboration. It was undoubtedly a dream come true.

I would also like to thank my co-supervisor Prof. Pedro Abreu for always having helpful and kind words and for the great influence in my academic life.

I would also like to thanks Dr. Vincent Andrieux for all the questions and excitement in my work and Prof. Carlos Rocha for helping me in the Geant4 and TGEANT simulation.

A special thanks to all my friends and colleagues in MEFT - "MEFT não se faz sozinho", without you MEFT would be a thousand times more impossible. Bernas, Miguel, Inês, Neves, Comboio, Filipa, Zeca, Manel, Zé, and Tânia thank you for all the afternoons/nights studying and partying. Bernas, Miguel and Comboio, my BFFs, thank you for being always there and for keeping me sane during COVID-19. You are definitely the best thing MEFT gave me.

To my ESN family, thank you for allowing me to be part of something bigger, although you could have given me less work while I was writing the thesis.

I would also like to thank my twin sister Bea, we grew up side by side and even during thesis time we suffered together, but we did it! But really, thank you for always being there for me and the cats.

To my mom, my brother, and my grandparents, who always supported me and allowed me to dream bigger and reach higher.

Last but not least, an enormous thanks to Tomás, you were crucial in always keeping me sane, feeling supported, and loved. Thank you for all the weekends, the trips, and the years together. Thank you.

A significant part of the work in this thesis was performed under the project CERN/FISPAR/0016/2021, designated "Collaboration in the COMPASS and AMBER Experiments at CERN".

Resumo

AMBER é uma experiência futura de alvo fixo no CERN. Foi aprovada recentemente e um dos objetivos de física da primeira fase é o estudo do processo Drell-Yan induzido por um pião. O processo Drell-Yan consiste na aniquilação de um quark e um antiquark originando um fotão virtual que decai no estado final para um par de leptões com cargas opostas. Este processo garante um acesso privilegiado à estrutura do pião. Desta forma, a contribuição da valência, do mar e dos gluões no pião serão caracterizadas com precisão sem precedente. AMBER usará feixes de piões de alta intensidade e energia, de ambas as cargas, a interagir com diferentes alvos nucleares. A configuração experimental de AMBER é baseada na da experiência COMPASS, introduzindo upgrades significativos ao espectrómetro já existente. Assim, a otimização da região do alvo de AMBER para as medidas de Drell-Yan está a ser estudada e é o objetivo deste trabalho. Neste trabalho, introduzimos uma cadeia de simulação de Monte Carlo. Começamos por simular o processo físico, seguido pela simulação do espectrómetro e da resposta dos detetores e termina na reconstrução dos dados obtidos. Assim, vamos estudar o impacto da introdução de detetores de vértice e como diferentes posições, geometrias e segmentações afetam os resultados. Neste estudo, o detector de microstrips de silício FVTX parece a opção mais sólida para o detetor de vértice. A escolha baseia-se nos valores obtidos para a resolução em massa e na posição Z do vértice, assim como na aceitância global de dimuões.

Palavras-chave: Experiência AMBER; Drell-Yan; Simulação de Monte-Carlo; Detetores de Vértice.

Abstract

The AMBER experiment is a future fixed-target experiment at SPS, CERN. It was recently approved, and one of the first phase physics goals is to study the pion-induced Drell-Yan process. The Drell-Yan process is a hard process where a quark-antiquark annihilation originates a virtual photon that decays in the final state to a pair of oppositely charged leptons. This process allows privileged access to the pion structure. At AMBER the valence, sea, and gluon contributions in the pion will be characterised with unprecedented accuracy, using high-intensity pion beams of both charges impinging in different nuclear targets. The AMBER setup is based on the COMPASS one but introduces significant upgrades to the existing spectrometer. Thus, the optimisation of the AMBER Drell-Yan detector is currently being studied and is a goal of this work. We introduce the AMBER Monte Carlo simulation chain. We start by simulating the physics process, followed by the simulation of the spectrometer and the response of the detector, and finally by allowing the reconstruction of the data. We will study the impact of the introduction of a vertex detector and how different positions, geometry, and segmentation affect the results. In our study, the silicon microstrips detector FVTX seems to be the most solid option. The choice is based on the values obtained for the dimuon mass and vertex position resolutions, as well as on the global acceptance for dimuons.

Keywords: AMBER experiment; Drell-Yan; Monte-Carlo Simulation

Vertex Detectors

Table of Contents

List of Tables

List of Figures

List of Abbreviations

AMBER Apparatus for Meson and Baryon Experimental Research.

CERN Conseil Européen pour la Recherche Nucléaire.

COMPASS Common Muon and Proton Apparatus for Structure and Spectroscopy.

CORAL Compass Reconstruction Analysis software.

DIS Deep Inelastic Scattering.

DY Drell-Yan.

EMC European Muon Collaboration.

FVTX Forward Vertex Detector.

LHC Large Hadron Collider.

MC Monte Carlo.

PDF Parton Distribution Function.

PDG Particle Data Group.

PHAST Physics Analysis Software Tool.

QCD Quantum Chromodynamics.

RHIC Relativistic Heavy Ion Collider.

SPS Super Proton Synchrotron.

VD Vertex Detector.

Chapter 1

The Drell-Yan Process

This chapter describes the Drell-Yan (DY) process. It starts by explaining the simple electromagnetic process, followed by including QCD diagrams into the process. It also introduces the concept of Parton Distribution Functions (PDFs) and their importance in understanding the dynamics within the pion. It also goes into detail on the nuclear dependences of this process.

1.1 Introduction to the Drel-Yan process

The first experimental study on lepton pairs produced in hadron-hadron scattering was done by Christenson *et al.* in 1968 [1]. This and more recent experiments show that hadron-hadron collisions produce a lepton pair mass spectrum as the one shown in Fig. 1.1. From around 4 to 8.5 GeV/c^2, there is a continuum, limited by the dashed vertical lines. In the same year, Sidney Drell and Tung-Mow Yan identified the mechanism responsible for this continuum observed as the Drell-Yan process [2].

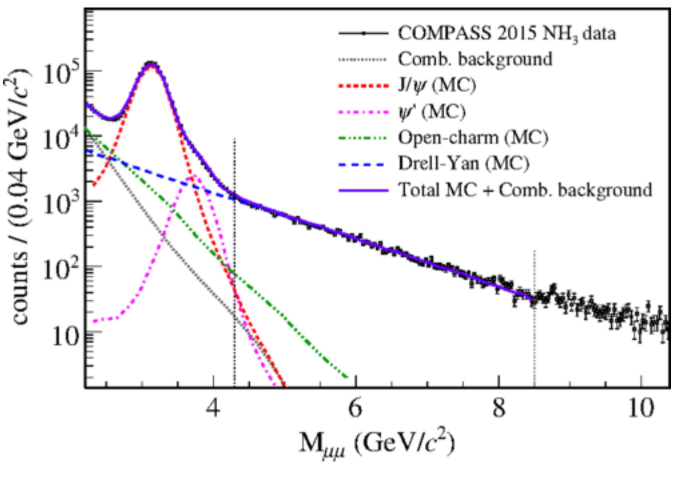

Figure 1.1: Dimuon invariant mass spectrum for a π^- beam at 190 GeV/c on ammonia target. Data collected in 2015 in the COMPASS Experiment at CERN, reproduced from [3].

Further interpretation of the mass spectrum reveals several contributions: the charmonia resonances (J/ψ, ψ') at masses 3.097 and 3.686 GeV/c^2 and semimuonic open-charm decays (D-mesons) for values of $M_{\mu\mu} \lesssim 6$ GeV/c^2, and combinatorial background of uncorrelated leptons, in addition to the DY process already referred to. The width of the resonances reflects the mass resolution of the experiment itself.

1.1.1 The Simple Drell-Yan Process

Drell-Yan (DY) is a rare process in which a quark and an antiquark annihilate and create a virtual photon (or a Z boson) that then decays into a pair of oppositely charged leptons. We are interested in studying the case when a virtual photon decays into a pair of muon and antimuon as this is experimentally easier to identify. The pair of opposite-charge muons is often called "dimuon". The Feynman diagram for this process in leading order (LO) is presented in Fig.1.2.

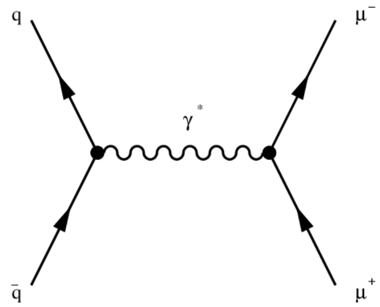

Figure 1.2: Feynman diagram for DY in LO.

1.1.2 Kinematics of the DY process

In a pion-induced DY, a charged pion (a meson with valence quarks $u\bar{d}$ for π^+ or $\bar{u}d$ for π^-) interacts with a nucleon, resulting in a pair of muons produced as follows:

$$\pi^{\pm}(P_\pi) + N(P_N) \rightarrow \gamma^*(q) \rightarrow \mu^+ + \mu^- + X \tag{1.1}$$

The relevant kinematic variables that describe the process are as follows:

$s = (P_\pi + P_N)^2$	the total centre-of-mass energy squared
$x_F = \left.\frac{P_{z\gamma*}}{P^{max}_{z\gamma*}}\right\|_{CMS} = \left.\frac{P_{z\gamma*}}{\sqrt{s}/2}\right\|_{CMS} \approx x_\pi - x_N$	the Feynman variable
$x_{\pi/N} = 0.5\left(\sqrt{x_F^2 + \frac{4Q^2}{s}} \pm x_F\right)$	the Bjorken x, the momentum fraction carried by a parton from $\pi^\pm/N$
$M^2_{\mu\mu} = Q^2 = q^2 = s x_\pi x_N$	the invariant mass squared of the dimuon.

where P_π (P_N) is the four-momentum of the beam (target) and q is the four-momentum of the virtual photon. The properties of the dimuon produced allow us to infer information about the hadrons that collided.

The differential cross section for this process depends on the momentum distribution of the quarks within the hadrons involved. According to [2], the pion-nucleon Drell-Yan cross section can be written as:

$$\frac{d\sigma}{dQ^2} \propto \sum_{i,j}\int_0^1 dx_\pi dx_N f_i(x_\pi, \mu_f) f_j(x_N, \mu_f)\hat{\sigma}_{ij}(z, \mu_r, \mu_f) \tag{1.2}$$

where the sum runs over all parton flavours in the pion (i) and the nucleon (j), $f_{i,j}$ are the parton distribution functions (PDFs). In this expression, μ_r and μ_f are the renormalization and factorisation scales, and $\hat{\sigma}_{ij}$ the partonic cross section, which depends on the ratio $z = Q^2/\hat{s}$, with $\sqrt{\hat{s}}$ being the partonic centre-of-mass energy and Q the four-momentum of $\gamma*$. The partonic centre-of-mass energy is related to the hadronic centre-of-mass energy $\sqrt{s}$ by the expression $\hat{s} = q^2 = x_1 x_2 s$. Here, the PDFs carry crucial information as they describe the internal structure of the hadrons. The PDF $f_i(x)$ can be interpreted as the probability distribution of finding a quark i with a fraction of momentum x from the parent hadron. The PDFs will be described in greater detail in section 1.3.

1.2 The DY Process in QCD

The predictions of the leading order DY process are in agreement with the experimental observations, with some exceptions.

1.2.1 QCD first order corrections

The cross-section measured (σ_{exp}) is larger by a factor of two with respect to the DY cross-section computed in leading order. To understand this result, it is necessary to improve our process model from the lowest order (the simple electromagnetic interaction) to one that considers Quantum Chromodynamics (QCD) processes leading to the same final state. Taking into account the first-order QCD diagrams, shown in Figure 1.3, we choose the first term in the perturbative expansion of the coupling constant α_s, obtaining the following:

$$\alpha_s\left(Q^2\right) = \frac{12\pi}{(33-2f)\ln\left(Q^2/\Lambda^2\right)} \tag{1.3}$$

where f denotes the number of quark flavours and Λ the interaction scale ($\sim$ 200 MeV/c). When taking Q as the typical dimuon mass value, the α_s value comes out small ($\sim$ 0.2), which shows that the perturbative expansion is appropriate. In the works of Altarelli, Ellis and Martinelli (1979) [4] and Parisi (1980) [5], they performed explicit calculations of the cross-section using next to leading order (NLO) diagrams and predicted that:

$$\sigma_{NLO} = K\sigma_{LO}, \tag{1.4}$$

where σ_{LO} denotes the cross section obtained at leading order and K represents the K-factor. They obtained $K \sim 1.6$ and $\alpha_s \sim 0.3$. The computation becomes very hard for higher orders since many Feynman diagrams are involved. Despite this, it was discovered that for the dominant vertex correction diagram, the perturbative series would exponentiate at:

$$K_{theo} \to \exp\left(\frac{2\pi\alpha_s}{3}\right) = 1.8. \tag{1.5}$$

It implies that most of the discrepancies between theoretical calculation and experimental measurements of the cross-section are explained by QCD first-order diagrams.

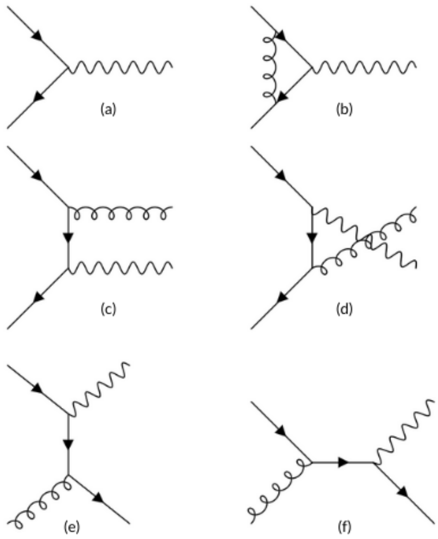

Figure 1.3: First order Feynman diagrams for the Drell Yan process. (a) Naive formulae DY diagram (b) Vertex correction diagram (c) and (d) initial state gluon emission (e) and (f) QCD Compton diagrams.

In Table 1.1, the experimental values obtained for K_{exp}, where $\sigma_{exp} = K_{exp} * \sigma_{LO}$, from various experiments are summarised. It is observed that the results obtained are of the order of 2 or bigger.

Experiment	Beam - Target	$\sqrt{s}$ (GeV)	K
NA50 [6]	$p - p$	29.1	$2.27 \pm 0.06 \pm 0.16$
E288	p - Pt	27.4	1.7
E439	p-W	27.4	1.6 ± 0.3
CHFMNP	$p - p$	44.6	1.6 ± 0.2
AABCSY	$p - p$	44.6	1.7
NA3	p - Pt	27.4	$3.1 \pm 0.5 \pm 0.3$
E537	$\bar{p}$ - W	15.3	$2.45 \pm 0.12 \pm 0.20$
NA3	$p, \bar{p}$ - Pt	16.8	2.3 ± 0.4
	$\pi -$ Pt	16.8	2.49 ± 0.37
	$\pi -$ Pt	22.9	2.22 ± 0.33
E326	$\pi -$ W	20.6	$2.70 \pm 0.08 \pm 0.40$
NA10	$\pi -$ W	19.1	2.8 ± 0.1
Goliath	$\pi -$ Be	16.8, 18.1	2.5
Omega	$\pi -$ W	8.7	2.6 ± 0.5

Table 1.1: Experimental values obtained for K factor.

1.3 Parton Distribution Functions

As mentioned before, the PDFs describe the way the momentum of a hadron is partitioned among its constituent partons. The proton PDFs have been extensively studied throughout the years. In Fig. 1.4, we have the most recent global fits for proton PDFs, considering NLO corrections. These global fits consider the available data from many different types of experiments, from hadron colliders and e^+e^- colliders to DIS experiments, in order to obtain a "prediction" for the flavour-dependent PDFs as a function of x, and their evolution with Q^2. Considering the range $x > 0.1$, achievable by fixed target experiments, we observe a remarkably precise description of each contribution for all x values.

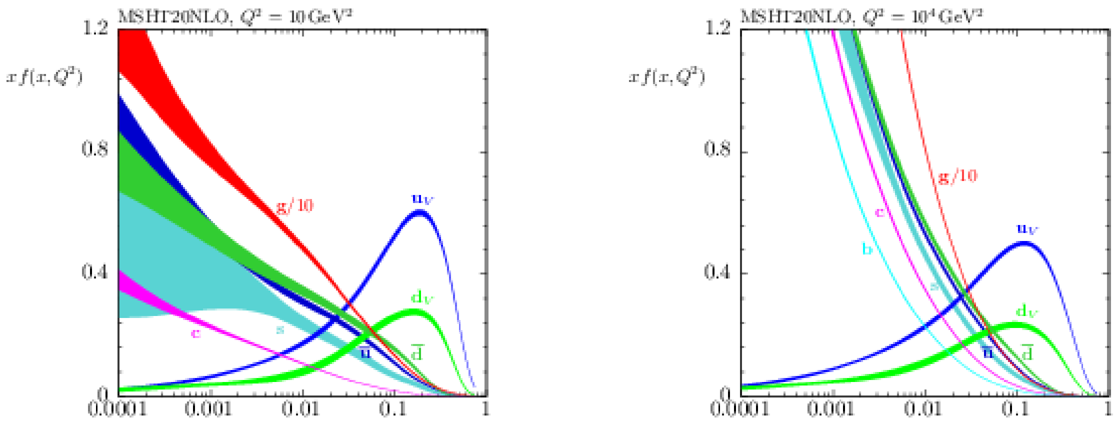

(a) At scale Q^2 =10 GeV. **(b)** At scale $Q^2 = 10^4$ GeV.

Figure 1.4: Proton Parton Distribution Functions for $Q^2 = 10$ GeV and $Q^2 = 10^4$ GeV. The bands are x times the unpolarized parton distributions f(x) (where f= u $_V$,d$_V$,u,d,s$\approx \bar{s}$,c= $\bar{c}$,b= $\bar{b}$,g) obtained in the NLO MSHT20 global analysis, reproduced from [7].

For the pion PDFs, much less information is available, thus a few assumptions are taken. We can summarise its extraction into three parts: determination of the valence-quark, sea-quark, and gluon contribution. The most direct way to access information on the pion valence structure is the pion-induced Drell-Yan process. We can extract the pion PDF by computing the DY cross section and the target distribution function. Data from this process were collected by the experiments mentioned in Table 1.1. The ones with the largest statistics, which published their differential cross-section measurements, were the NA3 [8] and NA10 [9] collaborations at CERN and the E615 [10] collaboration at Fermilab, more than 30 years ago. For the gluon component, other reactions, like direct-photon production in a hadron-hadron collision, allow us to impose constraints. WA70 [11] and NA24 [12] experiments obtained the available data from this reaction. NA3 used both π^+ and π^- beams to induce Drell-Yan. A combination of these DY cross sections allows separating the valence from the sea contribution in the pion. Fig. 1.5 shows global analyses focused on the pion structure.

Both SMRS [13] and GRV/S [14, 15] rely on the π^- DY data from E615 and NA10, as well as the direct-photon measurements of WA70 and NA24. For SMRS analysis, there are three curves for the sea quarks and gluons components, corresponding to three different hypotheses, where they assume that the sea quarks carry 10%, 15%, and 20% of the pion momentum fraction. In 2018, the JAM Collaboration [16] extracted pion PDFs using the same old pion-induced DY and direct photon production data and added the leading neutron electroproduction data from the HERA collider and new Monte-Carlo-based framework of analysis. This figure also shows the distributions for sea and valence quarks obtained by NA3 and the respective error band. The results obtained from these analyses do not agree and show the need for more precise data and better global analyses. The COMPASS collaboration has been working on the DY 2015

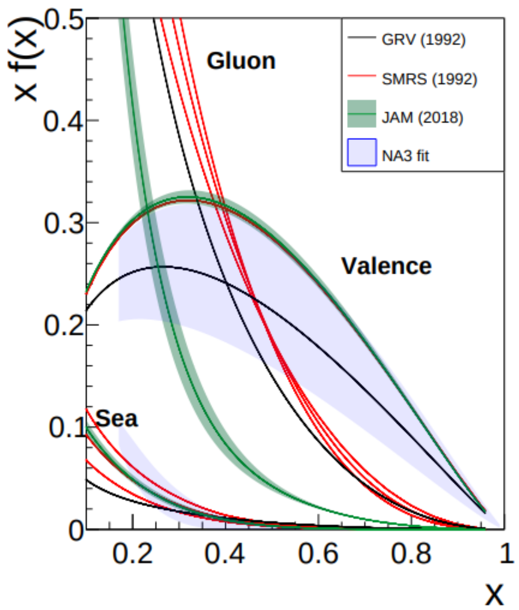

Figure 1.5: Valence, sea and gluon distributions for the pion from global fits of SMRS [13] GRV/S [14, 15] and JAM [16], at $Q^2 = 20$ GeV^2, shown together with the NA3 extraction [8], reproduced from [17].

and 2018 data; therefore, new results for the DY differential cross-section should be published soon. This, combined with the JAM analysis' method, might improve the global fits for the pion PDF.

As seen in Table 1.1, these experiments used nuclear targets, allowing us to also study the nuclear dependencies in a pion-induced DY.

1.4 A-dependence of Muon Pair Production

The nuclear dependence of a hadrons collision cross-section can be related to the simpler cross-section on nucleon by a simple relation to the mass number A [18]:

$$\sigma(\pi A) = \sigma_A(\pi N) \times A^{\alpha}, \tag{1.6}$$

where N refers to the nucleon. It is expected that $\alpha \sim 2/3$ for the hadronic inelastic cross-section and around 1 for the Drell Yan cross-section.

The α parameter is calculated by using the measurement of cross sections σ_{A_1} and σ_{A_2} of two nuclei with a mass number A_1 and A_2 respectively (with $A_1 < A_2$):

$$\alpha\left(A_2/A_1\right) = \frac{\ln\left(\frac{\sigma_{A_2}}{\sigma_{A_1}}\right)}{\ln\left(\frac{A_2}{A_1}\right)} \tag{1.7}$$

This parameter α is process-dependent and is often used as a measurement of the nuclear dependence of a given process. For Drell-Yan it was observed a long time ago that the alpha is much larger than for inelastic collisions. The DY alpha parameter was measured at FermiLab with a proton beam at 400 GeV/c on platinum and beryllium targets (for $M_{\mu\mu}$ between [5,11] GeV/c^2); at the NA3 for both pion beam charges on H_2 and Pt targets. A summary of the various values calculated for α:

$$
\begin{aligned}
\alpha_{\text{Fermilab}} &= 1.007 \pm 0.018 \text{ (stat.) } \pm 0.028 \text{ (sys.) } [18] \\
\alpha_{\text{NA3}} &= 1.03 \pm 0.03 \left(\pi^{\pm} \text{ on Pt/H}_2\right) [19] \\
\alpha_{\text{CFS}} &= 1.02 \pm 0.2 \,(\text{p on Pt/Cu/Be}) [20] \\
\alpha_{\text{CIP}} &= 1.12 \pm 0.05 \left(\pi^{-} \text{ on Pt/Cu/Be}\right) [21]
\end{aligned}
\tag{1.8}
$$

Several mechanisms were proposed to give a physics interpretation for the relatively large DY-alpha value, which all together are referred to as "Cold Nuclear Matter effects". Some of these will be briefly described in the next subsection.

1.5 Cold Nuclear Matter

Cold nuclear matter can be studied in hadron-nucleus collisions or DIS from fixed target energies ($\sqrt{s} \sim GeV$) to collider energies ($\sqrt{s} \sim TeV$).

EMC Effect

In 1983, the EMC (European Muon Collaboration) collaboration observed, for the first time, that the measured cross section per nucleon on light nuclear targets was different from that on heavy nuclear targets [22]. This effect is known as the EMC effect, which states that the quark and gluon PDFs in nucleons bound inside nuclei differ from those in free nucleons. This effect has been extensively studied throughout the years, however, there is still no model that thoroughly explains it.

Parton Energy Loss Effect

When a parton crosses a nuclear medium, it radiates gluons leading to energy loss. This effect is induced by rescattering in the medium, which can be a cold medium like a nucleus or a hot and deconfined medium like a quark-gluon plasma.

Cronin Effect

The Cronin effect was discovered in proton-nucleus collisions in 1975 [23]. The effect observed was a broadening of the transverse momentum distribution in proton-nucleus collisions, relative to proton-proton collisions. It arises from the multiple scatterings of proton partons off nucleus partons. They obtain a transverse momentum kick, shifting their momenta from lower to higher values. Although a qualitative understanding of the Cronin effect is provided, the transition between the energy region of fixed-target experiments and the one in RHIC and LCH is not well understood.

The AMBER collaboration proposes to measure pion-induced DY using both beam charges, in order to do valence and sea separation of the pion PDFs. It also introduces a carbon target and a tungsten one, where these nuclear effects can be studied.

Chapter 2

The AMBER experiment

2.1 Motivation

The AMBER (Apparatus for Meson and Baryon Experimental Research) collaboration proposes a "New QCD facility at the M2 beam line of the CERN SPS" [17]. AMBER will continue and extend the studies done by the presently ongoing COMPASS experiment [24], with a great variety of measurements on fundamental issues of Quantum Chromodynamics. The unique CERN SPS M2 beam line delivers hadron or naturally polarised $\mu^{\pm}$ beams in the energy range between 50 GeV and 280 GeV, allowing AMBER to address three major physics programmes in the first phase:

- Measurement of the proton-radius using elastic muon-proton scattering;
- Study Drell-Yan and charmonium production using conventional hadron beams;
- Measurement of antiproton production cross sections for the interpretation of Dark Matter searches.

For the second phase, AMBER intends to have a radio frequency-separated hadron beam, in particular, kaon and antiproton beams of high intensity and high energy. This unique feature will allow us to investigate several topics, such as:

- kaon structure from Drell-Yan, charmonium, and direct-photon production;
- kaon polarisabilities from Primakoff reactions;
- kaon spectroscopy: there are a dozen predicted states from the kaon sector still to be observed.

AMBER was approved by CERN in December 2020. Since then, there has been already a test run dedicated to the measurement of the proton charge radius in 2021, and a pilot run will happen at the end of 2022. The AMBER planning includes two months of antiproton production cross-section measurement in proton-Helium collisions, with a scan on the beam energies, in 2023. The muon-proton elastic scattering measurement will take close to two years (considering 140 effective days of measurement per year), in 2023 and 2024. This thesis focusses on the DY physics programme, which is scheduled to start in 2025.

2.2 Proposed Experimental Apparatus

The experimental apparatus planned for the AMBER measurements on the pion-induced Drell-Yan process is presented in Fig. 2.1. It is the common setup for a fixed-target experiment, where we have a target where the beam will interact, followed downstream by many detectors. In particular, for Drell-Yan measurements this setup includes a large hadron absorber after the target and upstream from the spectrometer detectors, to reduce the hadronic background. This setup is based on the COMPASS experiment [25] but significant upgrades to the existing spectrometer are planned [17]: from new front-end electronics to high-rate-capable CEDARs (Cherenkov Detector with Achromatic Ring Focus) able of running in triggerless mode and a new vertex detector system in the target region. The apparatus extends 60 metres downstream of the target and 50 metres upstream of it, roughly.

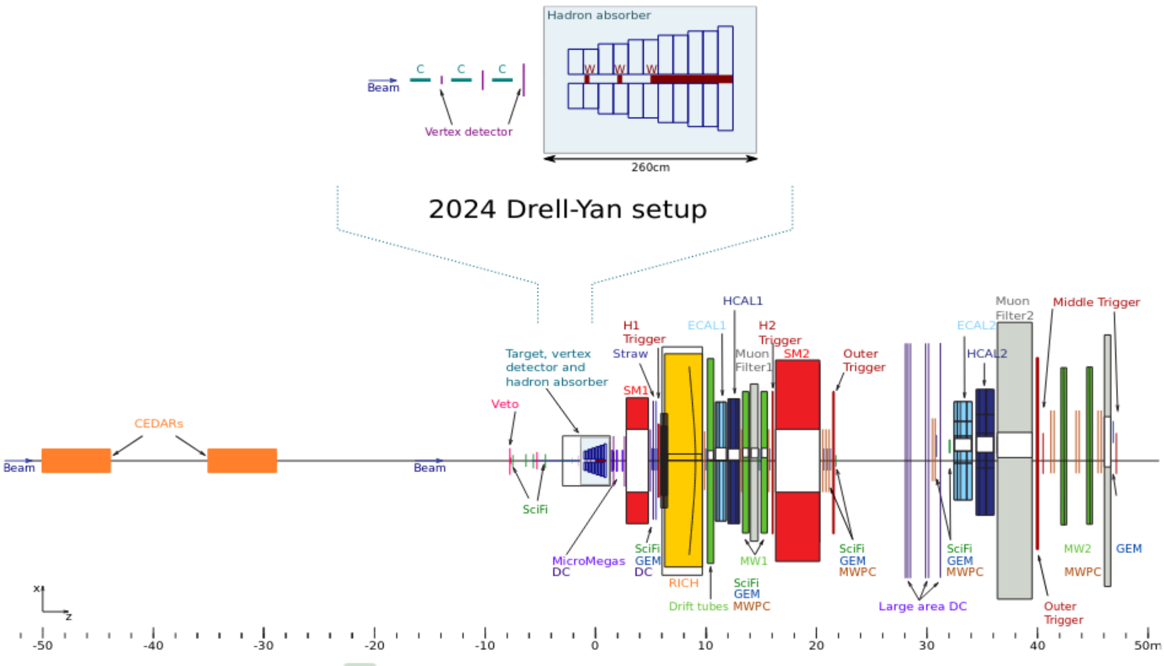

Figure 2.1: Experimental setup for the proposed Drell-Yan and charmonium measurements, reproduced from [17].

2.2.1 Beam

The beam delivered to fixed-target experiments from the SPS (Super Proton Synchrotron) accelerator at CERN is quantised in "packages" called spills or bursts. The SPS super-cycle and spill length may vary depending on the requirements of the experiments. A typical supercycle lasts 30 seconds with 2 extractions (spills), lasting 5 seconds each. Within the spill, the beam intensity is constant ("flat top").

The primary proton beam from SPS at 400 GeV/c is divided into several beamlines for fixed-target experiments. In the M2 beamline, the proton beam is scattered on a primary beryllium target (T6), whose thickness can be varied according to the desired beam intensity. It produces secondary hadron beams with protons, antiprotons, kaons, and pions, whose charge and momentum are then selected by quadrupole, dipole magnets and collimator obstacles. The secondary beam will pass through a long tunnel, where a significant fraction of the pions decays each into a muon and a neutrino. The DY physics program uses hadron beams, therefore, the muons are removed using another array of magnets. The hadron beams can be positively or negatively charged. The former comprises π^+, protons, and K^+, and the latter their antiparticles.

AMBER proposes the measurement of pion-induced Drell-Yan, at 190 GeV/c, using both pion charges, with an intensity that goes up to 10^8 hadrons per second. Fig. 2.2 shows the different hadron compositions for positive and negative beam charges as a function of the beam momentum, while Table 2.1 shows the relative beam composition for 190 GeV/c.

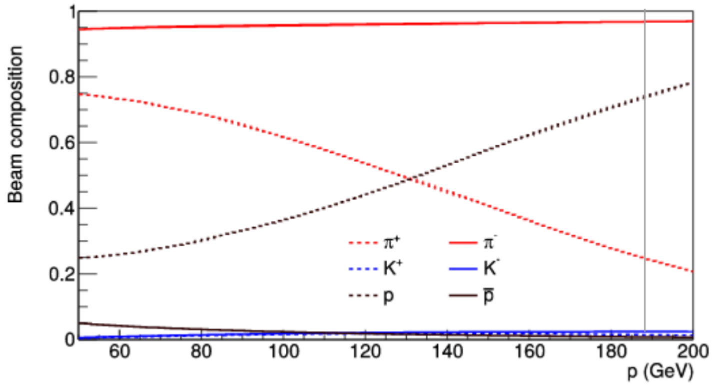

Figure 2.2: The composition of the hadron beam for different momenta, reproduced from [17]. The dashed lines correspond to the positively charged hadron beam, while the full lines correspond to the negatively charged beam. The vertical grey line is used to locate the beam momentum for the DY physics program (190 GeV/c).

Positive			Negative		
p	π^+	K$^+$	$\bar{p}$	π^-	K$^-$
74.6%	24.0%	1.4%	0.8%	96.8%	2.4%

Table 2.1: Relative composition for the hadron beam at 190 GeV/c.

With these hadron beams, not only pion-induced Drell-Yan is produced, but also kaon-induced and proton(antiproton)-induced reactions. The negative beam is mainly composed of π^-, therefore, contamination from K^- and $\bar{p}$ can be considered a negligible systematic error. On the other hand, π^+ constitute only 24.0% of all positively charged hadron beams, where protons contribute almost 74.6%.

It is crucial to identify the DY events induced by pions, therefore, one of the upgrades proposed is the high-rate CEDARs, differential Cherenkov counters placed in the M2 beam line. The purpose of such detectors is to identify the beam particle type event by event. The high rate capability is crucial since the beam intensity will be very high, allowing maximum DY statistics collection.

2.2.2 Target Region

For the target region, the AMBER proposal expresses the need for a vertex detector system, while proposing the target configuration presented in Fig. 2.1. It consists of three carbon cells with planes of the vertex detectors (VDs) in between them, followed by the hadron absorber with a tungsten target inside. More recently, after several Drell-Yan group meetings, the setup design for the target region was updated due to recent simulations. In this study, the most recent configuration for the target region is taken into account, as presented in Fig. 2.3.

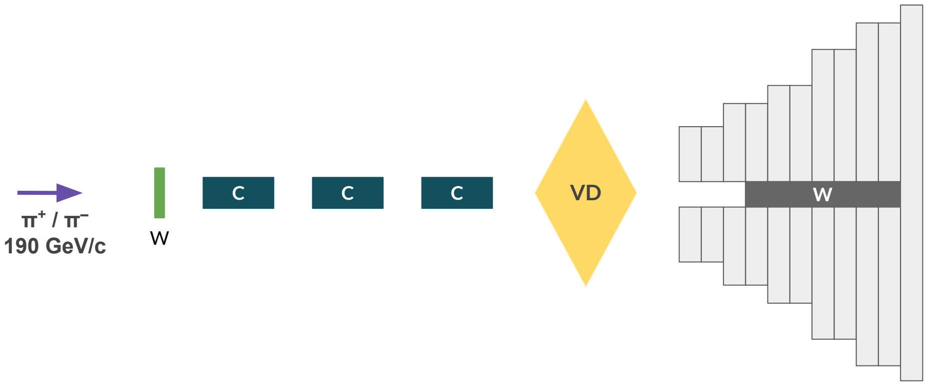

Figure 2.3: Target region composed of a tungsten cell (W) and a segmented carbon target (C), followed by vertex detectors (VD) and the hadron absorber (with a tungsten beam plug).

A target made of carbon and another made of tungsten are proposed. The first material is a light isoscalar, while the second one is a heavy material, allowing the study of nuclear-dependence effects. The tungsten cell is very thin, only 2 cm long, and is placed at the most upstream position, while the carbon cell is segmented into three sections, each 25 cm long.

Following the target, the dedicated vertex system will be added, resulting in a more precise reconstruction. The placement and characteristics of these vertex detectors are currently being studied and will be addressed in more detail throughout this project.

After that, a hadron absorber will be placed, reducing the secondary particle flux throughout the spectrometer. As previously stated, this physics programme intends to study muons as final-state particles. The absorber prevents the hadrons produced from occupying and sometimes even damaging the detectors at the beginning of the spectrometer, thus enabling the use of high-intensity pion beams. With such a beam, we need to ensure that we have an absorber that maximises the number of interaction lengths crossed by the hadrons while minimising the radiation lengths, so that muon multiple scattering and energy loss are minimal.

2.2.3 Large Angle Spectrometer (LAS)

LAS ensures an angular acceptance from 25 to 165 mrad to the polar angle of the outgoing muons (opening angle with respect to the beam direction), thus enabling the measurement of particles typically with high angle and low momentum. LAS is constructed around the first dipole magnet (SM1), a 110cm long magnet with a 229×152 cm^2 central opening. It produces an integrated field of 1.0 Tm., with the main component being the vertical one.

Additionally, LAS is composed of many tracking detectors, such as Pixel Micromegas (PM), Gas Electron Multipliers (GEMs), drift chambers (DC), straw detectors (ST), and multi-wire proportional chambers (PA). Aside from the tracking detectors, a Ring Imaging Cherenkov (RICH) detector is also part of the LAS, allowing for the identification of charged hadrons. LAS also includes an ECAL and an HCAL, both calorimeters, one to detect electromagnetic particles and the other the hadronic ones. In the end, LAS has a Muon Filter and hodoscopes.

2.2.4 Small Angle Spectrometer (SAS)

As the name says, SAS is used to detect particles with a small angle (from 8 to 45 mrad) with respect to the beam axis and thus high momentum. Similarly to LAS, it is also built around a dipole magnet, SM2, which has a rectangular shape with a length of 4 m and an opening of 2×1 m^2. When operated with a current of 5000 A, as is the case for the 190 GeV/c beam, the total field integral from SM2 is 5.13 T m. There are also tracking detectors such as Gas Electron Multipliers (GEMs), Micromegas (MM), Drift Chambers (W45) and MWPCs (PBs and PS). The ECAL2 and HCAL2, the electromagnetic and hadronic calorimeters, respectively, follow downstream before arriving at a Muon Filter 2 (MB) and the hodoscopes.

2.2.5 Muon Filters

The task of identifying muons is done in the Muon Wall stations. The filters include an absorber wall and two sets of tracking stations, one before the wall and one after. The absorber will stop background particles like hadrons, and thus only the muons trajectory will be reconstructed before and after.

These detection stations are called Muon Walls, with moderate spatial resolution. The first Muon Wall (MW1 or MA) is located downstream of SM1, in LAS. It consists of two stations of mini drift tubes (MDTs). Between the two stations, there is a 60 cm thick iron absorber (Muon Filter 1). The second Muon Wall (MW2 or MA) is in the final section of SAS. It comprises a 2.4 m thick concrete absorber (Muon Filter 2) followed by two MW2 stations and three MWPC stations. The trajectory of the particles before and after the muon filter is reconstructed also using the other trackers in SAS.

2.2.6 Trigger System

A trigger system is used to select the events of interest for the DY measurements. This system is crucial for the measurement, given the much lower DY events rate as compared to the hadronic inelastic events rate by a factor of a million. The dimuon trigger guarantees that only interesting events candidate to be of Drell-Yan origin are recorded, avoiding saturating the acquisition system.

Although the DY trigger for the AMBER experiment has not yet been established, there is a desire to reuse part of the COMPASS hodoscope trigger system. The dimuon trigger system is based on single muon triggers in time coincidence. As the SM1 and SM2 dipoles have a vertical field orientation, the charged particles are bent only in the horizontal plane. For this reason, the trigger is made of horizontal slabs that "measure" in the vertical direction (straight line trajectories in the YZ plane). The two hodoscopes from a pair have a target pointing capability, meaning that only slab combinations that point to the target are allowed to fire the trigger (in a so-called trigger matrix coincidence).

The single muon trigger is built up from 3 hodoscope subsystems: LAS, Outer and Middle. The details about each single muon trigger follow:

- **LAS trigger** is made of two hodoscope planes, H1 and H2, with 32 horizontal slabs each. They are located one upstream from the RICH and another downstream from MW1 (and before SM2).
- **Outer trigger** consists of two detection planes, namely HO3 and HO4. The first is made up of 18 horizontal slabs and is located immediately downstream of SM2, while the second is divided into two parts (left/right) with 16 horizontal slabs each.
- **Middle trigger** is composed of two stations, HM04Y1 and HM05Y1, with 32 horizontal slabs each and located at the end of the SAS region.

All hodoscopes have a central dead region (rectangular hole), to avoid triggers produced by muons from pion beam decays.

The three dimuon triggers are:

- LAS $\bigotimes$ LAS;
- LAS $\bigotimes$ Outer;
- LAS $\bigotimes$ Middle;

The LAS $\bigotimes$ Middle was not used for the COMPASS DY 2018 data taking, because it was seen to be still highly polluted with muons from pion decays. The AMBER Drell-Yan trigger system is still being defined, but its preliminary design considers running in triggerless mode (no level-0 trigger). Instead, one intends to have an online analysis of the hodoscope signals, which are treated by FPGA logics to build a level-1 dimuon trigger.

2.3 Vertex Detectors

The vertex detectors (VDs) will allow to improve the vertex position resolution, thus clearly separating events that originated in tungsten from those that originated in carbon. It will also improve the dimuon mass resolution. As can be inferred from Figure 1.1, this will reduce the smearing of the resonances into the high-mass Drell-Yan region, allowing us to lower the mass cut above which the Drell-Yan contribution is considered pure. This improvement impacts on the achievable statistics. The placement of these vertex detectors is still under study and will be discussed in this work.

The dimensions of the VDs have not yet been established and can range from 10 x 10 to 40 x 40 cm^2. The AMBER Collaboration is currently studying the type of technologies to use as target-region tracking planes. The options are scintillating fibres, silicon microstrips, or pixel silicon sensors. The AMBER proposal leaves this search for the suitable detector type open for the moment, since there are various criteria to consider, such as the cost and the spatial and time resolutions granted by such technology. The spatial resolution must be adequate to accurately reconstruct the particles' trajectory and the vertex position, while a good time resolution allows us to separate each event. The last feature is of extreme relevance: the M2-beam line provides quite intense beams, producing many secondary particles that will flood such detectors. Currently, we are studying two options for the material and geometry of the VDs. It is then crucial to rely on existing COMPASS data and to perform extensive Monte Carlo simulations with the new AMBER setup to evaluate the most advantageous option.

2.3.1 Silicon Pixel Detector

One of the options consists of silicon pixel detectors. They are usually composed of highly segmented sensors. The ALPIDE chip is currently being used in the ALICE experiment at CERN [26] and is being followed by the AMBER Proton Radius Measurement group to build a Unified Tracking Station that includes ALPIDEs and Scintilating Fiber detectors. Such a solution could be a good candidate for the VDs. At ALICE, the dimensions of the pixels used are $\sim$ 27 x 29 $(\mu m)^2$, and the detector itself is cylindrical, which is appropriate for a collider experiment. The important characteristics are shown in table 2.2.

Parameters	**Values**
Sensor thickness (μm)	50
Pixel Dimensions (μm^2)	27 $\times$ 29
Chip Dimension (mm^2)	15 $\times$ 30
Time resolution (μs)	30
Strip columns per plane	96
Max Particle fluence (MHz/cm^2)	100

Table 2.2: ALPIDE Pixel Sensor specifications, reproduced from [26].

For AMBER, we want a plane detector whose segmentation would be defined posteriorly, considering the cost of such technology and the spatial resolution needed. The more pixels each plane has, the better results we get when reconstructing the vertex position. However, this also entails additional costs due to the electronics and materials involved. The time resolution obtained using this technology is unsatisfactory and does not fulfil our experiment needs. If the ALPIDE chips are chosen as the most viable technology, it would have to be complemented by one or more scintillating fibre stations for a good reference in time.

In this work, we will simulate a general silicon plane detector, segment the detector into different pixel sizes, and study its impact on the DY reconstructed distributions.

2.3.2 Forward Vertex Detector (FVTX)

Another option would be to use an already existing silicon microstrip detector, the detector FVTX from the PHENIX experiment at the accelerator RHIC, in the USA [27]. Fig. 2.4 shows that the detector is composed of 4 planes separated from each other by 6 cm. They have a circular geometry with an inner radius of 4.4 cm and an outer radius of 16.9 cm and are segmented in both the radial and in the ϕ directions.

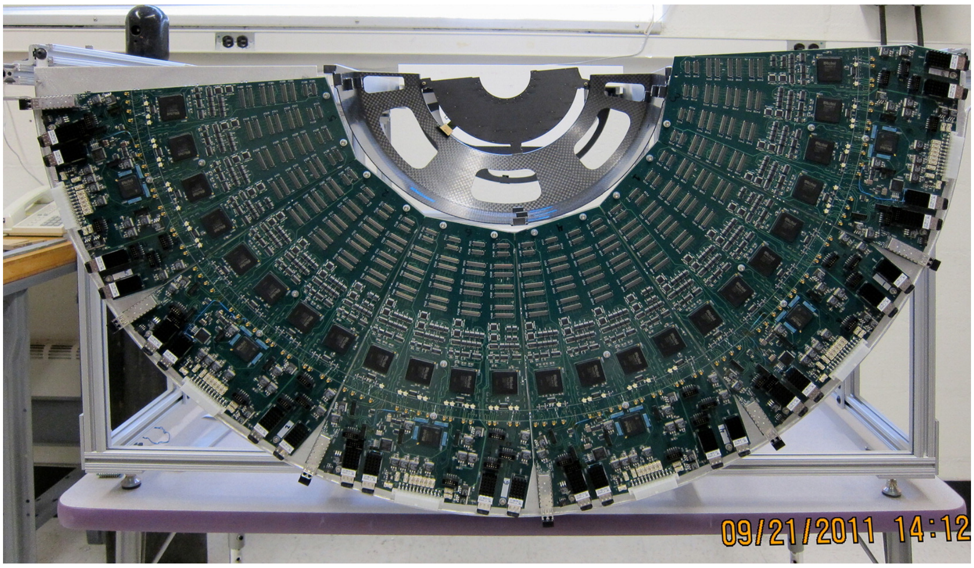

Figure 2.4: Photo of an FVTX half plane, reproduced from [27]. It is noticeable the segmentation in ϕ direction.

The microstrips have a size of 75 μm in the radial direction, and the length increases with the radius from 3.4 mm (in the inner radius) to 11.5 mm (in the outer radius), with each column covering 3.75°. The relevant FVTX features are presented in Table 2.3.

Parameters	Values
Silicon sensor thickness (μm)	320
Strip pitch (μm)	75
Strips per column	1664
Inner radius (mm)	44.0
Strip columns per plane	96
Time resolution (ns)	10

Table 2.3: FVTX Specifications, reproduced from [27].

This detector has fixed dimensions and segmentation that are not necessarily the best for the DY programme. The microstrips are of the order of millimetres, which would most likely grant a worse spatial resolution than the previous technology. The time resolution is appropriate ($\sim$ 10 ns). This detector would have to undergo several modifications and upgrades to meet the needs, but seems to provide an affordable option. Moreover, this option concedes a better time resolution than the ALPIDE pixel technology.

As mentioned before, we need to study these options with extensive MC simulations, which include adding both detectors to AMBER MC-chain (described in section 3) and analysing how it impacts the relevant DY kinematic distributions.

Chapter 3

Monte Carlo Simulation Study

To plan new experiments, one needs to perform extensive simulations of the experimental setup. The AMBER simulation chain comprises four fundamental steps, illustrated in Fig. 3.1. The first one is a simulation of the physics process using an event generator. In this study, we use PYTHIA 8 [28], a general purpose physics event generator written in C++, allowing us to understand high-energy physics interactions at leading and next to leading order and obtain the kinematic distributions that describe them according to a model. Following this, it is crucial to simulate the detector and its behaviour when particles propagate through it. In this sense, we use TGEANT [29, 30], a Geant4 [31] based program, where we mimic the entire detector in Geant4. TGEANT receives as input the events generated from PYTHIA8 and returns the information that the detector would produce under the simulated conditions. In addition to particle transport through matter, normal interactions are simulated, including multiple scattering, energy loss, particle showers, etc. Afterwards, we use CORAL to analyse the output from TGEANT. CORAL [32] is a C++ programme used for physics data reconstruction. It uses the information in the form of hits in detectors, energy deposits in calorimeters, etc., to reconstruct the particles' trajectories (tracking) and the vertices per event (vertexing). The CORAL output is then given to PHAST [33], a data analysis framework that allows us to access both the simulated truth (from PYTHIA 8 / TGEANT) and the reconstructed information.

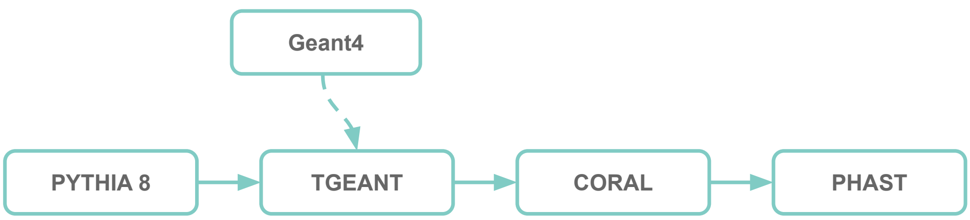

Figure 3.1: AMBER Monte Carlo simulation chain.

3.1 Simulation of the DY process

The software PYTHIA 8, version 8.2.40, is used to simulate the DY process. It considers the Feynman diagrams of the requested process, in LO or up to NLO, and uses the PDF sets provided as input, generating several high-energy physics interactions.

Generation Parameters

It is necessary to set some generation parameters for this particular simulation in PYTHIA. The ones used in this work are described as follows:

- the process considered is $f + \bar{f} \to \gamma^*/Z^0$. Due to the limited centre-of-mass energy of these interactions at AMBER, the Drell-Yan is dominated by γ^* in this case;
- the γ^* decay products considered are muons, so that $\gamma^* \to \mu^- + \mu^+$. Although the virtual photon can decay into leptons, or $q\bar{q}$ pairs, we select the final state with dimuon;
- regarding the beam, we define this experiment as a fixed target one, with a π^- beam with 190 GeV/c interacting with a proton or neutron at rest.
- for the dimuon mass range, it is considered $3.5 < M_{\mu\mu} < 11$ GeV/c^2;
- processes like initial- and final-state radiation (the so-called parton showers) are turned on, allowing gluon emission through the generation.
- for the PDFs, LHAPDF [34], a package linked with the PYTHIA libraries, is used. The selected PDF sets are GRVPI1 for the pions, while NNPDF23_nlo_as_0119 is used for the protons.
- by tunning the partons k$_T$ distribution parameters, we are able to reproduce the dimuon p_T distribution obtained from the real data (in the DY mass range [4-9] GeV/c^2).

Regarding the mass range, we needed to guarantee maximum statistics while considering only the DY process. Considering Fig. 1.1 that was obtained by the COMPASS experiment, there is a substantial contribution from J/Ψ and Ψ' in the [2-4] GeV/c^2 mass range. For mass values larger than 9 GeV / c^2, there is also a Υ family contribution. We conclude that the desired DY mass range is [4,9] GeV/c^2. Setting the lower limit to 3.5 GeV/c^2 and the upper limit to 11 GeV/c^2, gives a margin to accommodate the large smearing that will be introduced from the muons when crossing the hadron absorber. Even though this is the mass interval generated, there will be a few events below this range due to initial-state radiation and meson decays. Throughout the data analysis, we will implement the cut of [4,9] GeV/c^2 on the mass range.

Kinematic Distributions

200k events are generated in PYTHIA, to analyse the generated kinematic distributions of the dimuon. Fig. 3.2b presents its transverse momentum, while Fig. 3.2c its invariant mass. One characteristic of the

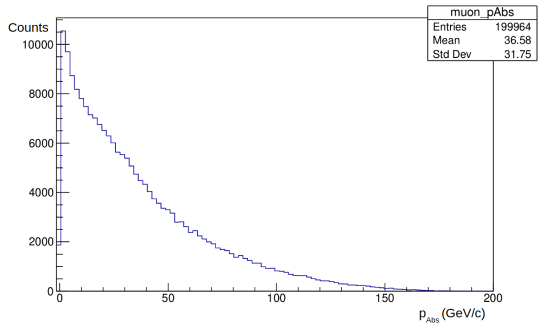

(a) Muon absolute momentum, obtained using PYTHIA 8.

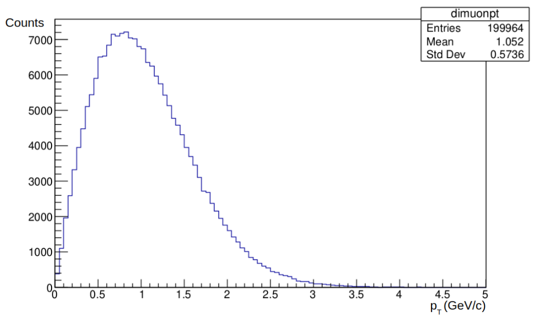

(b) Dimuon Transverse Momentum, obtained using PYTHIA 8.

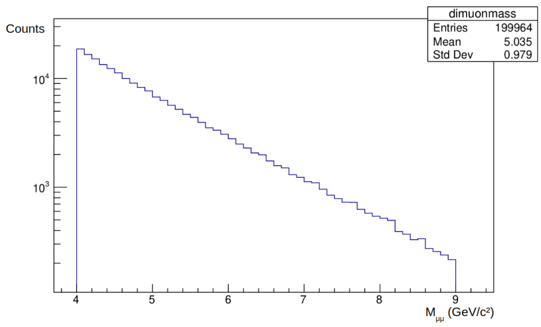

(c) Dimuon invariant mass, obtained using PYTHIA 8.

Figure 3.2: Kinematics distributions of interest in DY process.

DY process is the mean value for the dimuon p_T of around 1 GeV/c, which is corroborated by Fig. 3.2b, where we obtained $\langle p_T \rangle = 1.052$ GeV/c. In Fig. 3.2c, we can observe that, in the generated mass range $4 < M_{\mu\mu} < 9\ GeV/c^2$, the distribution has a decreasing exponential behaviour, the same tendency that is observed in real data, from Fig. 1.1.

3.2 AMBER Spectrometer Simulation

TGEANT is responsible for simulating the detector and its response in the AMBER Monte Carlo simulation chain. Before introducing TGEANT, we do a preliminary study of the target region proposed in this work using Geant4. This study does not directly relate to the simulation of the DY process in the proposed DY AMBER setup. Still, it gives us insight into other physics interactions that will occur as background.

3.2.1 Target Region in Geant4

A preliminary study is performed on the interactions produced by a single pion beam. As stated before, the Geant4 simulation accounts for particles that interact with matter (not rare processes such as DY). By analysing the data from such simulations, we will study events that will contribute to the background in our experiment.

Simulation

The target region of the AMBER experiment is simulated. It includes developing a complex code with several classes and describing the geometry, material, and interactions of the vertex detector. A summary of the various classes implemented is given below:

- **Primary Generator Action:** contains the class G4GeneralParticleSource that produces the beam made of one negative pion at 190 GeV/c along the z-direction;
- **Physics List:**: selects the physics processes that occur. We used FTFP BERT HP ("Bertini Cascade" model) that contains not only the standard electromagnetic processes but also the hadronic ones, such as nuclear de-excitation, neutron capture, gamma-nucleus and electron-nucleus interactions, and elastic and inelastic scattering.
- **Event Action** and **Run Action:** save the important variables in an output (a ROOT Tree in our case);
- **Detector Construction:** where all the targets and detectors are built. We introduce the materials and composites, then define the geometry, and place them in the mother volume.
- **Sensitive Detector** and **Pixel Hit:** are classes introduced by us that process and save each hit in the detector and its information.
- **VD Parameterisation**: also introduced by us, describing the segmentation of the detector.

Fig. 3.3 illustrates the geometry of the target region that resulted from such implementation. The targets are a thin cell made of tungsten followed by three long ones made of carbon. Three silicon planes are placed downstream of the targets, with 51 x 51 cm^2. These planes are segmented into chips of 1.5 x 3 cm^2. The materials used in the Vertex Detector and the chip's dimension follow the ALPIDE technology features mentioned in Chapter 2. The pixels themselves are not implemented at this level of the simulation.

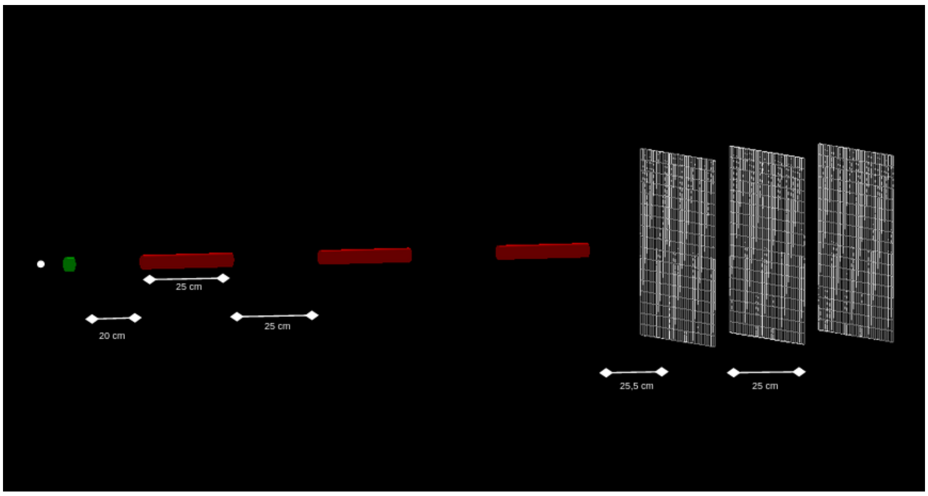

Figure 3.3: Implementation of the target region in Geant4. It is composed of the tungsten target (in green), the carbon target (red) and three segmented planes of the Vertex Detector.

It is important to note that this simulation is not exactly the same as the one done in AMBER's simulation chain. Even though the distances between targets and detector planes are almost comparable, they are not precisely equal. This serves only as an exercise.

Results

Fig. 3.4 shows an event with one beam particle and all the interactions that occur. Different colours show various species of particles, where can see the large amount of particles produced from a single beam particle. To analyse it further, we simulated 100K beam particles interacting. We start by looking at the final-state

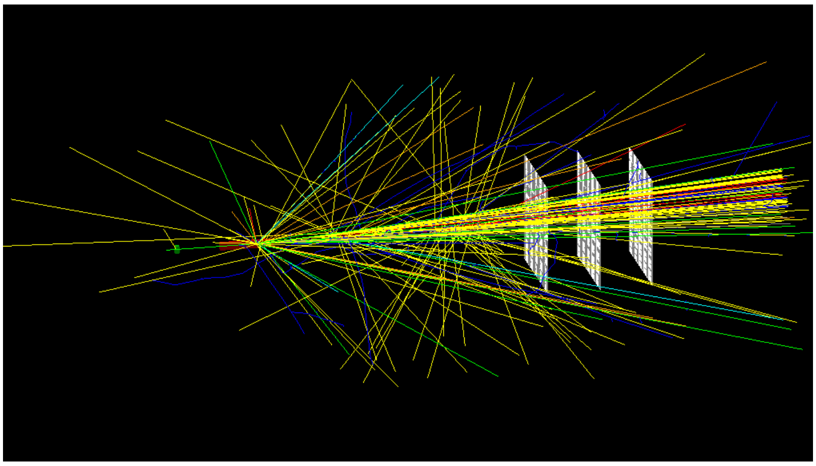

Figure 3.4: Simulation with one beam particle in Geant4. There are photons (yellow), electrons (blue), positrons (red), negative pions (green), and positive pions (orange) being produced.

particles that are produced and hit the first plane, selecting the particles that could be measured in a real experiment. The results are presented in Table 3.1, where we selected the type of particles that hit the detector the most and the muons since they are the particles of interest in this study. We see a high fraction

Particles	Amount
π^-	7.8%
π^+	8.9%
e^+	27.0%
e^-	52.0%
p	2.6%
μ^- / μ^+	0.30%

Table 3.1: Charged particles that hit the 1st VD - Geant4.

of electrons, products of ionisation that occurs in many instances as a result of the interaction of particles with the materials of the targets/detectors. Additionally, the total multiplicity of charged particles produced is also calculated, obtaining $\sim$63 particles/beam particle.

Another interesting preliminary study is related to the rate of particles that cross the detector, especially in the central area. In an actual experiment, if the particle flux is significantly high, the detector saturates and the events are not be recorded, making the detector unusable. Using the features of ALPIDE technology as reference, the maximum particle rate per cm^2 is 100 MHz.

To compare the produced particles rate with this reference, we need to do some calculations considering the number of events generated, the number of particles that hit the detector, and the beam intensity of our experiment (10^8 particles/s), as follows:

$$\frac{N_{VD}}{N_{events}} \times I_{beam}, \tag{3.1}$$

resulting in the number of particles that hit the first plane per second. In Fig. 3.5, we observe a 2D histogram of the first VD plane with a binning of 1x1 cm^2. With this, we can directly compare the values of each bin with the reference value of such a detector of 100 MHz per cm^2. The bin height (z-axis) was rescaled using the previous equation, corresponding to the number of particles that go through that plane per second. Consequently, there is only one place (1x1 cm^2) in the central zone where the obtained values are larger than 100 MHz, around $\sim$ 149 MHz. In this region, the detector would not be able to process all the particles that pass through, losing that information. Therefore, the introduction of a dead zone is to be studied in greater detail as it depends on the final position of the detector and the specific pixel size chosen.

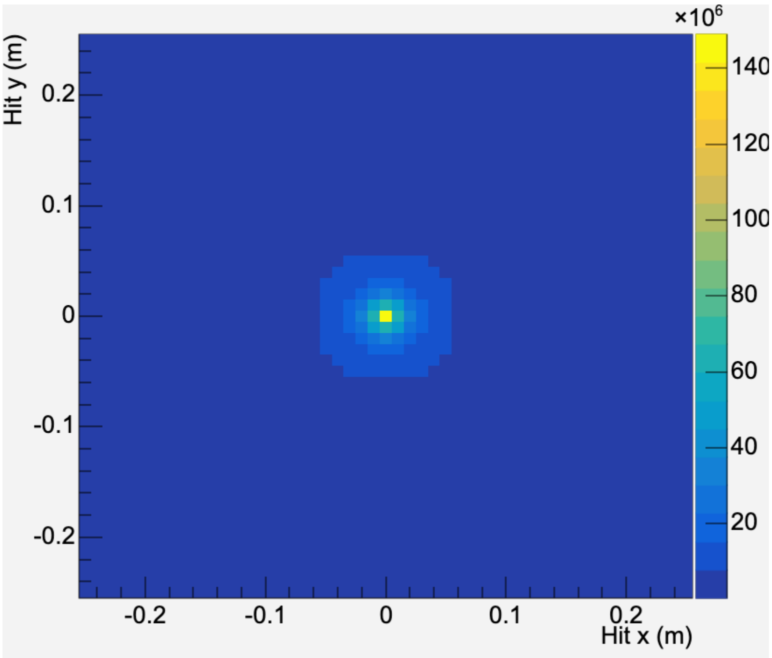

Figure 3.5: Rate of particles that cross the first VD plane per second by cm^2.

3.2.2 Whole Spectrometer in TGEANT

TGEANT is a software designed for COMPASS, which allows for the simulation of the entire spectrometer. Performs four major tasks: geometry description, particle propagation, physics interactions, and sensitive detector area definition. As input, the programme receives a settings file with the extension .xml, containing the placement of each detector as well as various generation features, i.e. the number of events to be simulated, the type and energy of the beam, which kind of outputs are to be created, the introduction or not of pile-up, production cuts, etc. This file also calls other ones as input:

- a PYTHIA tuning file that contains information about the event generation in PYTHIA8 as described in the previous section.
- a beam file containing information about the beam parameterisation from the measured data at COMPASS.
- a magnetic field map for the SM1 and SM2 dipole magnets.
- a .xml file with more information about the detectors' efficiency.

The types of outputs that TGEANT returns are *.tgeant, *.gdml, and *.dat. The first one contains the data of the Monte Carlo events throughout the spectrometer: the GDML file contains the geometry simulated; and the so-called "detectors.dat" has the specifications for each detector implemented, its dimensions, position, segmentation, radiation lengths of the material, efficiency, pitch, etc. The simulated geometry implemented in TGEANT of the DY AMBER proposal setup is presented in Fig. 3.6.

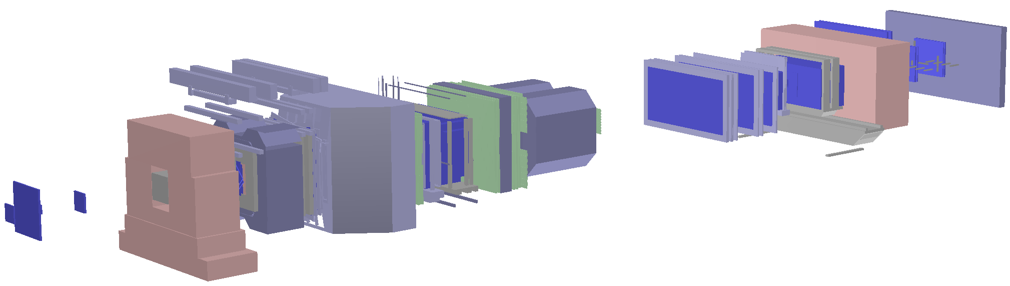

Figure 3.6: Implementation of DY AMBER proposed spectrometer in TGEANT.

Some of the implementations are highlighted, presenting additional information/calculations.

Target Region Implementation and Beam Attenuation

In the target region, it is placed a tungsten cell and a segmented carbon target. The material used in TGEANT for the carbon target is compact carbon. In Table 3.2, there is a summary of the placement and dimensions of the cells, where C1, C2 and C3 represent each carbon cell.

As the beam goes through each target, it becomes attenuated (absorbed). To study the probability of this

Cell	**Length** (cm)	**Radius** (cm)	Z_{center} (cm)
W	2	2	-318.5
C1	25	2	-280
C2	25	2	-230
C3	25	2	-180

Table 3.2: Features and position (Z_{centre}) of the target cells.

interaction, we introduce λ_{int}, the mean distance travelled by the pion before undergoing an inelastic nuclear interaction. Using equation 3.2, we calculate the fraction of particles that can go through the length x of a specific material.

$$\frac{N}{N_0} = \exp\left(-x/\lambda_{int}\right) \tag{3.2}$$

Consequently, the interaction probability is given by:

$$P_{int} = 1 - \frac{N}{N_0} = 1 - e^{-x/\lambda_{int}} \tag{3.3}$$

By using λ_{int} values mentioned in [35] for tungsten and compact carbon materials, we obtain that 83.8% of beam particles cross the 2cm long tungsten target without interacting. For the entire carbon target, we see that only 23.6% of the beam particles that reach it would cross it without interacting. If we now consider the target layout, i.e. the first cell being made of tungsten followed by three carbon cells, it is possible to arrive at the values presented in Table 3.3.

The remaining beam particles ($\sim 20\%$ of the initial beam intensity) will follow into the vertex detectors, the

Target	λ_{int} (cm)	**Length** (cm)	**Interaction probability of the initial beam particles**
W	11.32	2	16.3%
C	52.00	75	64.0%

Table 3.3: Interaction probability of the initial beam with each target.

hadron absorber, and a beam plug. The beam plug, placed along the beam direction, inside the absorber, and also made of tungsten, is used to avoid that this remaining beam will reach the spectrometer detectors.

To include the vertex detectors, the AMBER settings file used for TGEANT setup is changed. Three squared planes are introduced at Z-positions -150, -127 and -100 cm. They are 40 x 40 cm ^{2}, 30 μm thick and composed of silicon. The goal is to use a general detector that can be posteriorly segmented (during data analysis), giving a chance to compare the results with different pixel sizes and geometries.

Hadron Absorber Implementation and Multiple Scattering

The hadron absorber considered in this simulation is 220 cm long, with 200 cm of alumina (Al_2O_3) followed by 20 cm of stainless steel, and is shown in Fig. 3.7. It has a hole in the middle, where the beam plug is located. The main goal is to drastically reduce the beam particles that did not interact with the targets. It is made of tungsten and its length in these simulations is 120 cm.

To calculate the particles that cross the beam plug without interacting, we use equation 3.2 applied to the 120 cm of tungsten in the plug and we consider that only $\sim 20\%$ of the initial beam intensity reaches the hadron absorber. We find that the fraction $\sim 1.87 \times 10^{-6}$ of particles will cross the tungsten beam plug and the additional 20 cm of stainless steel without interacting. This is a low value; however, when considering the beam intensity as 10^8 π/s and the low DY cross-section value, we see that the non-interacting beam

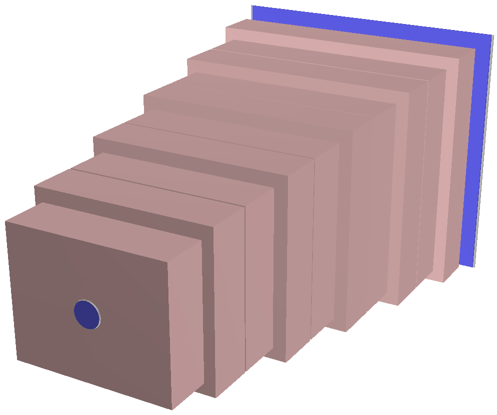

Figure 3.7: Implementation of the hadron absorber (in red Al_2O_3 and blue Fe) in TGEANT.

will still contaminate our DY measurements.[1]

There is also the need to minimise the multiple scattering and energy loss of the final-state muons when crossing the hadron absorber. Most of the detectors in the spectrometer are very thin, resulting in a very small disturbance to the muons. However, this is not the case for the absorber and therefore we need to take into account its length and materials. To study this, it is essential to introduce X_0, the radiation length of the material related to the energy loss of high-energy electromagnetic particles when crossing a specific material. It is the distance a muon can travel within a material until it loses an energy factor of $1/e$. Using the values presented in PDG [35] for each of the materials in the absorber, it is possible to calculate X/X_0, the number of radiation lengths each muon goes through when crossing each material. Relevant quantities are calculated and presented in Table 3.4 for each material.

	Material	ρ (g/cm^3)	**Length** (cm)	λ_{int} (cm)	X_0 (cm)	X/X_0
Absorber	Al_2O_3	3.97	200	32.56	7.038	28.417
	Fe	7.874	20	20.41	1.757	11.383
Beam Plug	W	19.3	120	11.32	0.3504	342.466

Table 3.4: Absorber and beam plug features and calculation of the radiation lengths crossed by a muon.

We also need to consider dE/dx, the energy lost by a muon when crossing a specific material by unit length. Depending on the range of momentum of the initial muons, we will have different values for dE/dx. We distinguish two cases: the muons that derive from the DY process and the muons that come from hadron decays. For the first ones, we want to be sure that the multiple scattering and energy lost when crossing the hadron absorber are minimal, whereas, for the second ones, we are primarily interested in maximising the hadrons' stopping power, since they may decay into muons, or reach the detectors. To obtain the correct

[1]The AMBER collaboration will study the possibility of extending the tungsten beam plug since there is still space available inside the absorber.

value for dE/dx, we take a quick look at the plots obtained afterwards using Phast. We check that the average momentum of a Drell-Yan muon before crossing the hadron absorber is around 45 GeV/c. For the muons produced by pion beam decays along the beam tunnel, that may reach the beam plug, we consider their average momentum of ∼190 GeV/c. Following this, we calculate the muon energy loss when crossing each absorber material, using Equation 3.4. The values obtained for the relevant quantities are presented in Table 3.5.

$$\Delta E = \frac{dE}{dx}\rho\Delta x \tag{3.4}$$

		dE/dx (MeV cm^2 g^{-1})	ΔE (GeV)	
p_μ=45 GeV/c	Al_2O_3	2.373	1.884	2.247
	Fe	2.302	0.363	
	W	2.164	5.012	5.374
p_μ=190 GeV/c	Al_2O_3	3.082	2.447	3.004
	Fe	3.536	0.557	
	W	4.567	10.577	11.134

Table 3.5: Energy loss of a muon when crossing the absorber and beam plug, for $\langle p_\mu \rangle$=45 GeV/c and $\langle p_\mu \rangle$=190 GeV/c, respectively.

From Tables 3.4 and 3.5, we verify that a DY muon loses around 2.25 GeV when crossing the absorber, while it travels around 40 radiation lengths. The muons produced in pion decays will have a small angle because of their high momentum and will go through the beam plug (around 343 radiation lengths), losing around 11.1 GeV.

We can verify the calculations made with the simulation results for the DY muons. In Fig. 3.8, we show

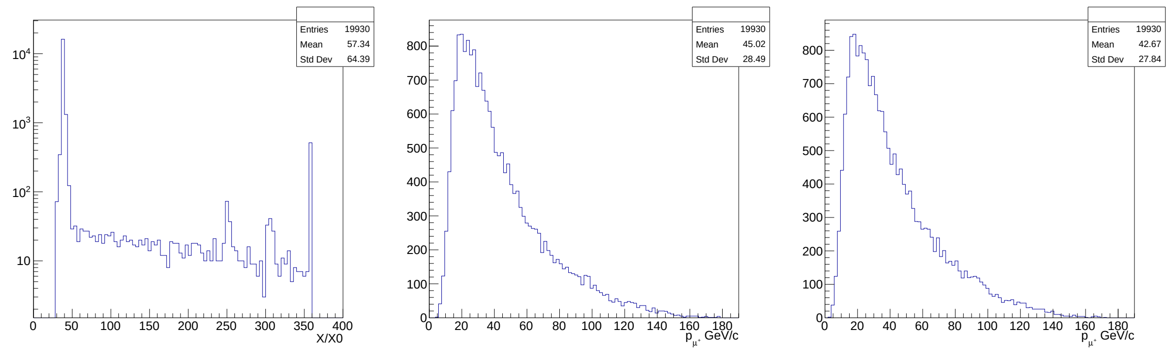

(a) X/X0 crossed from the first VD to the first detected hit.

(b) p_{μ^+} distribution in the first VD plane position.

(c) p_{μ^+} distribution in the first spectrometer hit position, downstream of the absorber.

Figure 3.8: Radiation lengths crossed by μ^+ when travelling through the absorber (a) and p_{μ^+} distributions before (b) and after it (c).

relevant distributions for μ^+. Starting with Fig. 3.8a, we observe that the radiation lengths crossed by the antimuon are, in most cases, around 40 radiation lengths, compatible with Table 3.4. There are some cases where the antimuons go through the beam plug, crossing around 350 radiation lengths. From the momentum distributions before and after the absorber in Figs. 3.8b and 3.8c, we can start by verifying that the typical p_μ is around 45 GeV/c, compatible with the value used before for calculating the DY muon energy loss. By subtracting the average momentum before the absorber from the one after, we recover a typical muon energy loss of around 2.35 GeV, which is consistent with our calculations.

3.3 Reconstruction of simulated events

With the simulated response of the detectors, we treat these data as experimental data and reconstruct the information using COMPASS Reconstruction Algorithm Software (CORAL) [24, 25, 32]. We provide "detectors.dat", the .gdml and the .tgeant files as input for CORAL. The software performs various operations: calculates the number of radiation lengths crossed by the particles in the spectrometer, links particles with calorimeter clusters, and fits interaction vertices and charged particle tracks. The track reconstruction algorithm has three main steps: it starts with pattern recognition (i.e. finding straight segments in zones of the spectrometer free from magnetic fields and dense materials); followed by bridging (i.e. connecting straight segments through magnets and absorbers); finally, we have fitting (i.e., computing the best track parameters, based on a Kalman Fit [36, 37].

During the reconstruction, it also attempts to make vertices out of the reconstructed tracks. We can have primary and secondary vertices for each event, whose reconstruction procedure is different. For the primary one, the vertexing process uses the beam track and all outgoing tracks, calculating the closest distance of approach between the beam and each of the reconstructed tracks. An inverse Kalman Fit is then performed, allowing us to exclude the tracks that significantly increase the fit χ^2. The secondary vertices are expected to be the product of the decay of neutral particles. In this case, tracks are searched with opposite charges, and a possible decay position of the unobserved neutral particle is computed. Multiple primary and secondary vertices may be reconstructed in an event. Therefore, the same track can be associated with more than one vertex. At the physics analysis stage, selecting the best primary vertex (i.e., the one with the best reduced χ^2) is possible.

As output, CORAL returns ROOT histograms, useful for studying detectors, and mDSTs (mini Data Summary Tapes), which collect information about reconstructed events in ROOT Trees [38].

3.4 Data Analysis

The last step of this analysis is to analyse the reconstructed events. PHAST is used for this purpose and can process the mDST file, providing a set of C++ classes to examine it. The code written by the user, the so-called user-event, gives us access to tracks, vertices, and the relevant parameters associated with them. As an output, PHAST can return a ROOT file with a Tree object, allowing access and manipulation of the information in it in a more flexible way.

For this analysis, 10 samples of 15000 events each were generated, resulting in 150000 events in total, saved into mDSTs.

3.4.1 Reconstruction Analysis

Before going into detail on the optimisation studies using a vertex detector, which is the main topic of this work, it is essential to analyse the DY events generated and reconstructed by MC with the standard spectrometer.

Geometrical Acceptance

For the 150K events generated, many final-state particles are generated among which the two opposite charge muons in each event. Part of these particles will not be detected on the spectrometer because the hadron absorber stops them or because the geometrical coverage of the detectors does not accept them. The following equation is used to calculate the geometrical acceptance:

$$a_{geo} = \frac{N_{MC-Acc}}{N_{MC}}, \tag{3.5}$$

where N_{MC} corresponds to the number of final-state particles generated and N_{MC-Acc} the number of final-state particles accepted within the spectrometer. To calculate the latter, we will select the particles that have a MC hit (i.e. by looking at the MC truth) in one of the hodoscopes since these are the ones that could have fired the trigger. With this, it is possible to calculate the geometrical acceptance for each part of the spectrometer. We can obtain the single muon's geometrical acceptance by doing this exercise for all the muons and antimuons produced. Table 3.6 shows the results obtained per spectrometer zone. In this table, all the muons reconstructed are included, regardless of their origin, i.e. both the muons from the Drell-Yan process and those from hadron decays are considered (although very few, in this simulation, which is done without pile-up).

The sum of geometrical acceptance values for LAS and SAS exceeds that of the entire spectrometer

Zone	a_{geo}
All	58.3 ± 0.2 %
LAS	44.3 ± 0.1 %
SAS	20.0 ± 0.1 %

Table 3.6: Geometrical acceptance for muons per zone of the spectrometer.

considered as a whole. This is a consequence of the overlap between the LAS and SAS hodoscopes that leads to some muons crossing both spectrometer zones. More than half of the muons generated are in the acceptance of the spectrometer. The acceptance is larger in the LAS, in accordance with the typically large angles at which Drell-Yan muons are emitted.

Reconstruction efficiency

From all the particles generated that are within geometrical acceptance, only some will be reconstructed. The reconstruction efficiency, ϵ_{rec}, can be calculated by comparing the number of reconstructed particle tracks with those generated and accepted. To do this, we look at the MC track of each muon and check if it was reconstructed. The values obtained in each spectrometer zone for the reconstruction efficiency of the muon (determined as the reconstructed particles that cross more than 30 radiation lengths between the first and last measured points on the spectrometer) are shown in Table 3.7. The reconstruction efficiencies for

Zone	ϵ_{rec}
All	82.1 $\pm$ 0.3 %
LAS	77.8 $\pm$ 0.3 %
SAS	69.6 $\pm$ 0.4 %

Table 3.7: Reconstruction efficiency per zone for the muons.

LAS and SAS are calculated with respect to the accepted muons in each spectrometer part. LAS presents a higher reconstruction efficiency, around 78%, while SAS presents one of around 70%.

Fig. 3.9 shows the momentum and θ_{lab} distributions of the reconstructed μ^+. The anti-muons detected in SAS have a small angle with $\langle\theta_{lab}\rangle$= 23.5 mrad, while those detected in LAS have larger angles, with the average value being $\langle\theta_{lab}\rangle$ = 72.3 mrad. For the momentum distributions, the μ^+ detected in SAS has a higher value, with their distribution starting around 20 GeV/c and the average value being $\langle p\rangle \sim$80 GeV/c. Those detected in LAS generally have a smaller momentum with $\langle p\rangle$ = 33 GeV/c. The distributions obtained agree with the description of each part of the spectrometer, discussed in Chapter 2.

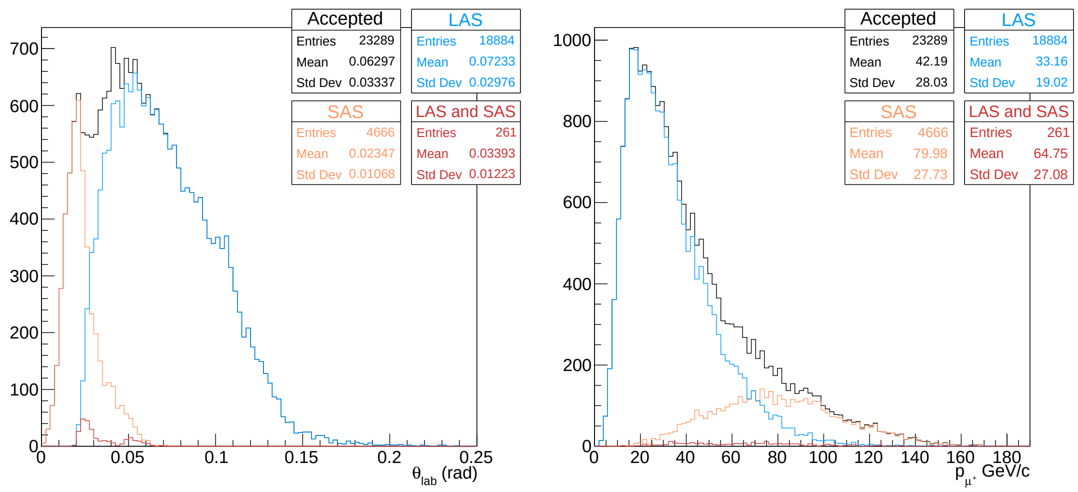

(a) μ^+ θ_{lab} distribution.

(b) μ^+ momentum distribution.

Figure 3.9: Distributions for μ^+ by single muon trigger type.

Dimuon Events

The dimuon events are those where two muons originate from the same primary vertex. For these events, we can study the geometrical acceptance and properties of the pair of muons involved. 55278 dimuon events are accepted from the 150000 generated. Table 3.8 presents an evaluation of the geometrical acceptance of the DY dimuon. By checking the MC hits on the hodoscopes created by both muons of the pair, we can verify the dimuon acceptance. This acceptance is relatively large for the dimuons in the mass range 4 to 9

GeV/c^2, in the order of 37%. We also observe that the acceptance is larger for LAS & LAS events than for LAS & SAS events.

Zone	a_{geo}
All	36.9 ± 0.2%
LAS & LAS	23.7 ± 0.1%
LAS & Outer	19.0 ± 0.1 %

Table 3.8: Dimuon geometrical acceptance per zone of the spectrometer.

3.4.2 Event Selection

From the 150K events generated, only 41780 are reconstructed with a dimuon with a vertex in common. Therefore, we have a reconstruction efficiency of 41780/55278 = 75.6%. In fact, it is not only the reconstruction efficiency, it is convoluted with the muon identification efficiency since the particle Id was selected. Several quality cuts are applied, similar to the ones usually applied to real data, as follows:

1. Two muons of opposite sign reconstructed on the spectrometer (with PID = 5 or PID = 6, which means that the particles are identified as muons);
2. The trigger bit corresponding to one of the dimuon triggers equal to one (either LAS $\bigotimes$ LAS; or LAS $\bigotimes$ Outer);
3. Each muon has the last measured point downstream of the Muon Filter 1 ($Z_{last} > 1500$ cm);
4. Each muon has the first measured point upstream of SM1 ($Z_{first} < 300$ cm);
5. Common vertex between the two particles is within the target limits. The target region is selected by $-319.5 < Z_{vtx} < -317.5$ cm for the tungsten target and $-292.5 < Z_{vtx} < -267.5$ cm , $-242.5 < Z_{vtx} < -217.5$ cm and $-192.5 < Z_{vtx} < -167.5$ cm for each carbon cell;
6. For each muon, the track must have a $\chi^2/ndf < 10$ to ensure the quality of the reconstructed tracks;
7. The reconstructed dimuon mass must be within [4,9] GeV/c^2.

Table 3.9 shows the impact of these cuts in the selected events.

	Cut	**Events selected**	**Percentage**
1	$\mu^- \ \mu^+$	41780	100 %
2	trigger	23961	57.4%
3	$Z_{last} > 1500$	23784	56.9%
4	$Z_{first} <300$	23055	55.2%
5	Z_{vtx} in targets	19939	47.7%
6	χ^2_μ/ndf < 10	19930	47.7 %
7	$4 < M_{\mu\mu} < 9$	11783	28.2%

Table 3.9: Impact of each selection criteria in the reconstructed events.

Dimuon events after selection cuts

After applying the selection cuts, it is important to study the impact on the DY kinematic variables. We introduce the variables and show the distributions of the generated, the generated within the geometrical acceptance, and the reconstructed events.
We start with the distribution of the dimuon mass, shown in Fig. 3.10. On the left side, Fig. 3.10a shows the distribution without cuts, confirming the dimuon mass generation range from [3.5,11] GeV/c^2. Events generated with masses lower than 3.5 GeV/c^2 are a product of final-state radiation for muons and combinatorial with muons from hadron decays, as mentioned earlier. On the right side, Fig. 3.10b shows the direct impact of the dimuon mass cut. The decreasing exponential behaviour seen in all curves is anticipated as shown in Fig.1.1 for this mass range.

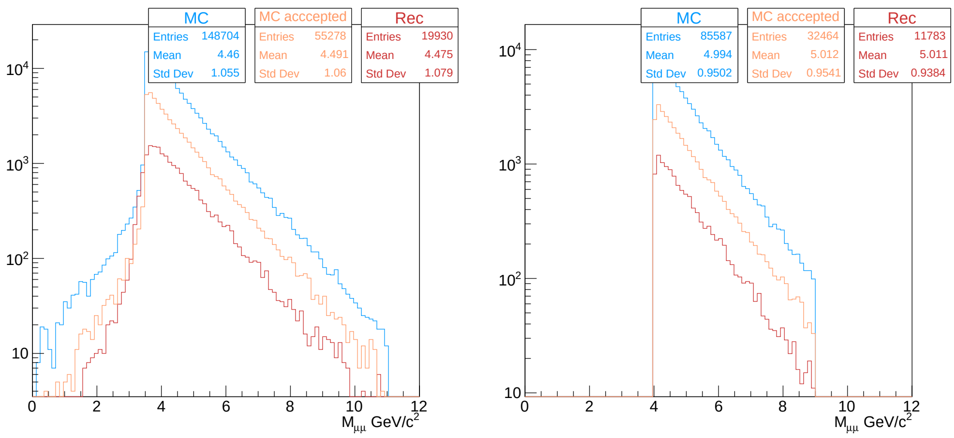

(a) No dimuon mass cut applied

(b) $4 < M_{\mu\mu} < 9$ GeV/c^2

Figure 3.10: Dimuon invariant mass distributions, considering generated, accepted, and reconstructed events.

Fig. 3.11 illustrates the Z-position of the primary vertex, Z_{vtx}. Using the MC Z_{vtx}, it is clear the position of each target cell, starting with the tungsten one followed downstream by the three carbon cells. For the reconstructed Z_{vtx}, the distribution is smeared around every target cell, especially the tungsten, whose size and position become almost imperceptible. This will be addressed in the next chapter with the introduction of the vertex detectors.

Fig. 3.12 displays the x_1 (previously named x_π), x_2 (previously named x_N) and x_F distributions. Only the events with $x_1 > 0.2$ are reconstructed, which also impacts the average values obtained, the generated sample has $\langle x_1 \rangle = 0.39$, while for the reconstructed one we have $\langle x_1 \rangle = 0.50$. For x_F, we can observe a higher acceptance and, therefore, a reconstruction fraction for positive values.

Regarding the dimuon transverse momentum distribution, displayed in Fig. 3.13, the curve is similar for all sets of events. The average value of these sets is around ~ 1 GeV/c and agrees with the distribution obtained in PYTHIA 8, presented in Fig. 3.2b.

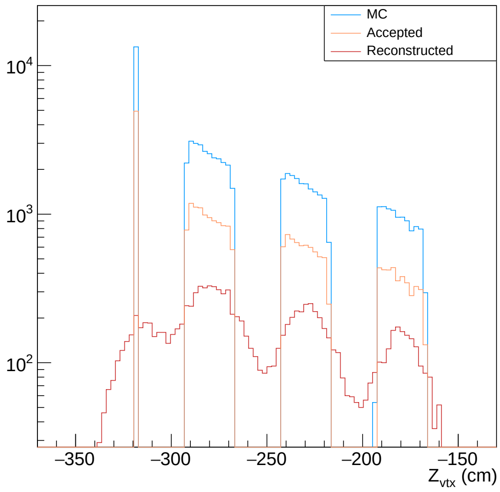

Figure 3.11: Z_{vtx} distributions for generated, accepted, and reconstructed dimuon pairs, within the dimuon mass range $[4, 9]$ GeV/c^2.

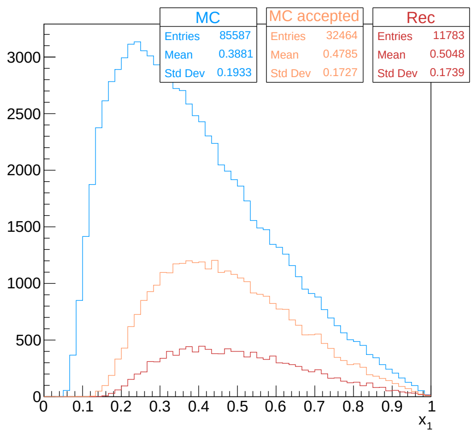

(a) x_1 distribution.

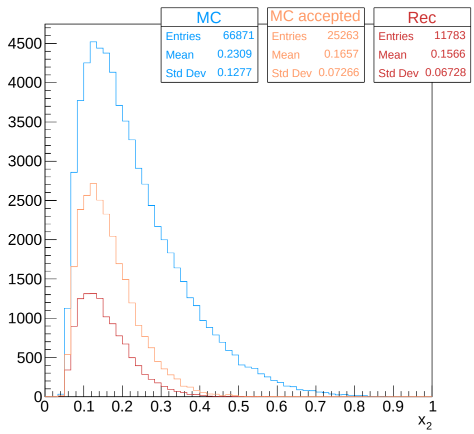

(b) x_2 distribution.

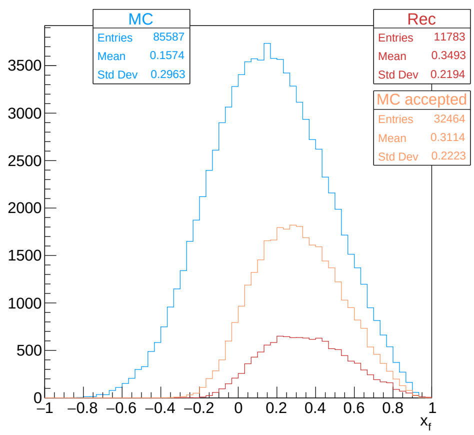

(c) x_f distribution.

Figure 3.12: x_1, x_2 x_f distributions, considering generated, generated and accepted, and reconstructed events.

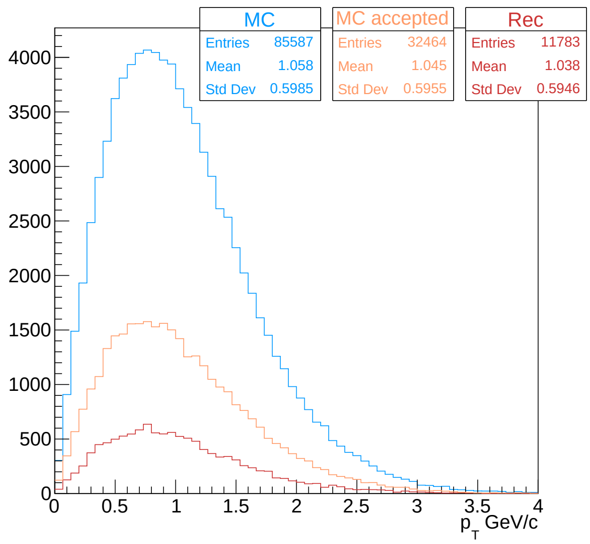

Figure 3.13: Dimuon p_T distributions for generated, generated and accepted, and reconstructed dimuon pairs.

Chapter 4

Optimisation Studies

The chapter starts with a deeper analysis of the DY kinematic variables and essential studies on acceptance and resolution, followed by the optimisation study of the vertex detector. It presents two different analysis, one with an ideal reconstruction while the other takes a realistic approach. Different VD segmentations, geometries and positions are simulated and studied.

4.1 DY Kinematic Distributions

Firstly, we detail the kinematic distributions presented in the last chapter, discussing key concepts such as global acceptance and resolution.

4.1.1 Acceptance

As explored in Chapter 3, the events generated may not be reconstructed. Global acceptance accounts for geometrical acceptance, trigger and detector efficiencies, and spectrometer resolution effects. We can calculate it as follows:

$$a_{global} = \frac{N_{rec}}{N_{MC}}, \tag{4.1}$$

by considering the generated and reconstructed events. The global acceptance of dimuons can also be examined per target, that is, by limiting the Z_{vtx} to each target position, shown in Table 4.1. Cuts in the dimuon mass and Z_{vtx}^{MC} are applied to the generated events. Reconstructed events undergo the cuts presented in Table 3.9, including the additional cut in the dimuon mass. The tungsten target presents a

	a_{global}
All	10.1 ± 0.1 %
W	1.3 ± 0.1 %
C1	11.4 ± 0.2 %
C2	12.9 ± 0.3 %
C3	13.9 ± 0.4 %

Table 4.1: Global acceptance for each target cell.

considerably low acceptance when the nominal limits of this target are considered. It is very thin (2 cm long), and our spectrometer's spatial resolution does not allow us to measure the Z-position so precisely, due to significant smearing around this target position, as shown before in Fig. 3.11. As we move further downstream, we conclude that the acceptance is increasing with Z.

It is also possible to evaluate the differential acceptance as a function of kinematic variables, such as the dimuon mass, as shown in Fig. 4.1. As seen in Fig. 4.1, the acceptance as a function of dimuon mass

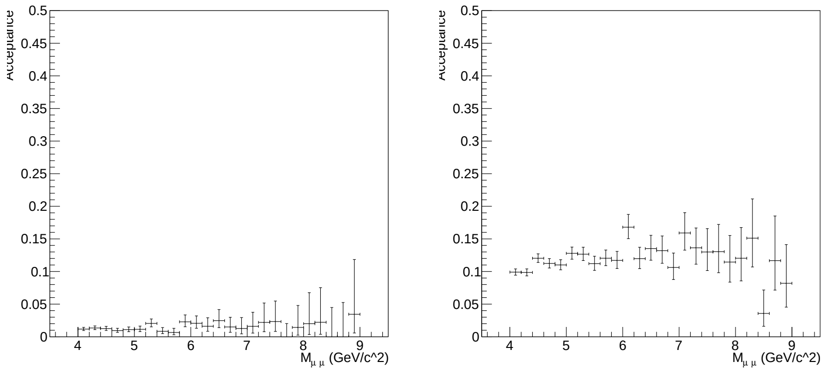

(a) $M_{\mu\mu}$ acceptance for the tungsten cell. **(b)** $M_{\mu\mu}$ acceptance for the first carbon cell.

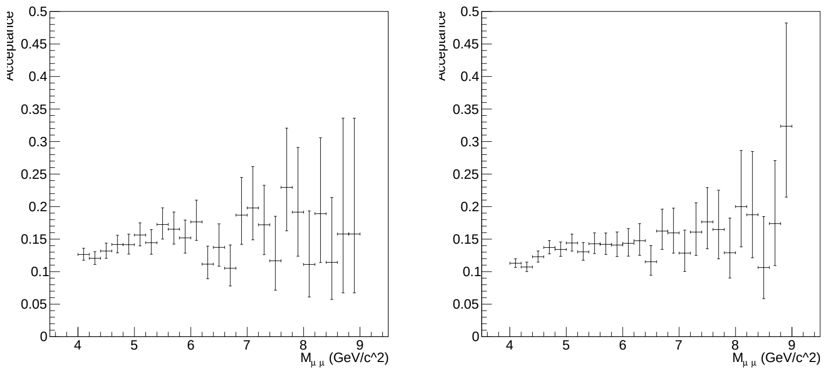

(c) $M_{\mu\mu}$ acceptance for the second carbon cell. **(d)** $M_{\mu\mu}$ acceptance for the third carbon cell.

Figure 4.1: Acceptance as a function of the dimuon mass for each target.

is nearly flat, around the values computed for the global acceptance, in Table 4.1. The acceptance as a function of x_1, x_F and p_T for each target is also studied, where we combined the distributions of the three carbon cells since a similar trend is expected. The transverse momentum acceptance is presented in Fig. 4.2, which is also nearly flat. For higher p_T values, we have fewer events, so we observe more considerable uncertainties. The x_1 and x_F acceptance plots are presented in Fig. 4.3. When x_F is lower than -0.2, acceptance is zero, as expected, since most of the reconstructed events are for positive x_F values.

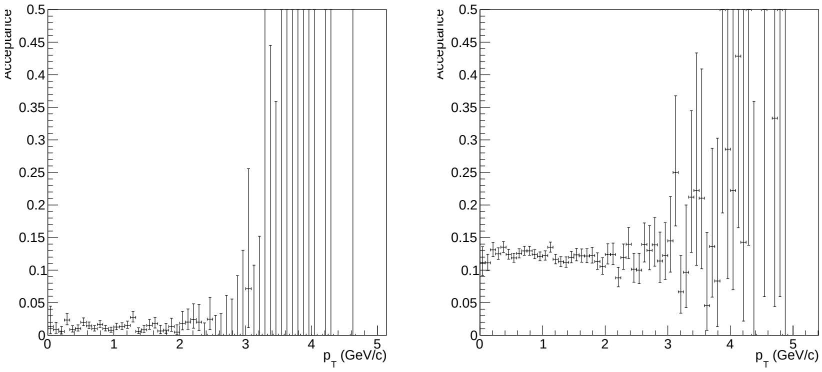

(a) p_T acceptance for the tungsten cell. **(b)** p_T acceptance for the carbon cells.

Figure 4.2: Acceptance as a function of the dimuon transverse momentum for each target.

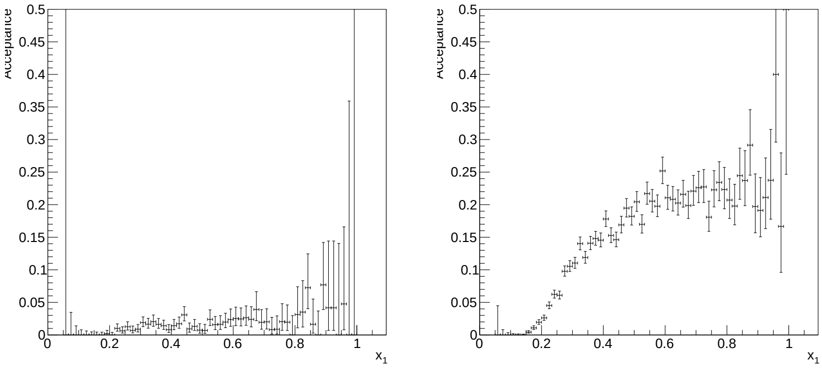

(a) x_1 acceptance for the tungsten cell. **(b)** x_1 acceptance for the carbon cells.

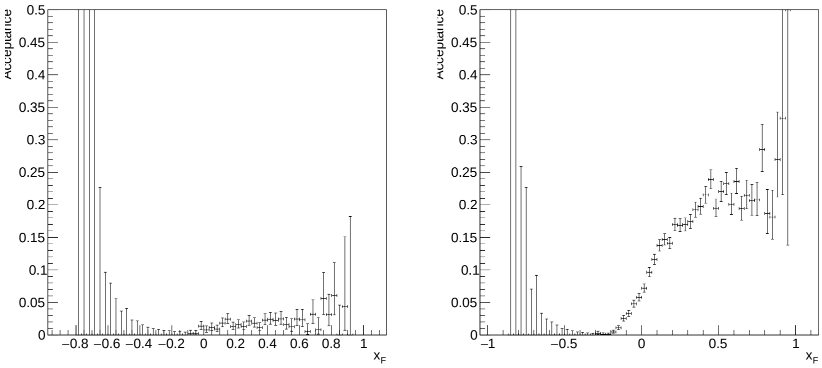

(c) x_F acceptance for the tungsten cell. **(d)** x_F acceptance for the carbon cells.

Figure 4.3: Acceptance as a function of the x_1 and x_F for each target.

4.1.2 Resolution

It is possible to associate the reconstructed track with the corresponding generated one. For example, if the track has been reconstructed at a given position, Z_{rec}, the associated generated track will be at Z_{mc}. The difference between these two positions is related to the resolution effects of the spectrometer. Thus, the ΔZ_{vtx} is calculated as follows:

$$\Delta Z_{vtx} = Z_{vtx}^{rec} - Z_{vtx}^{MC}. \tag{4.2}$$

The resolution is obtained by calculating the standard deviation of the ΔZ_{vtx} distribution. It is crucial to study the resolution per target since we expect different spatial resolutions for each target cell, as shown in Fig. 3.11. These distributions are fitted with a simple Gaussian, where its σ represents the resolution of the distribution and the measurement. The plots obtained are presented in Fig. 4.4. We observe that the

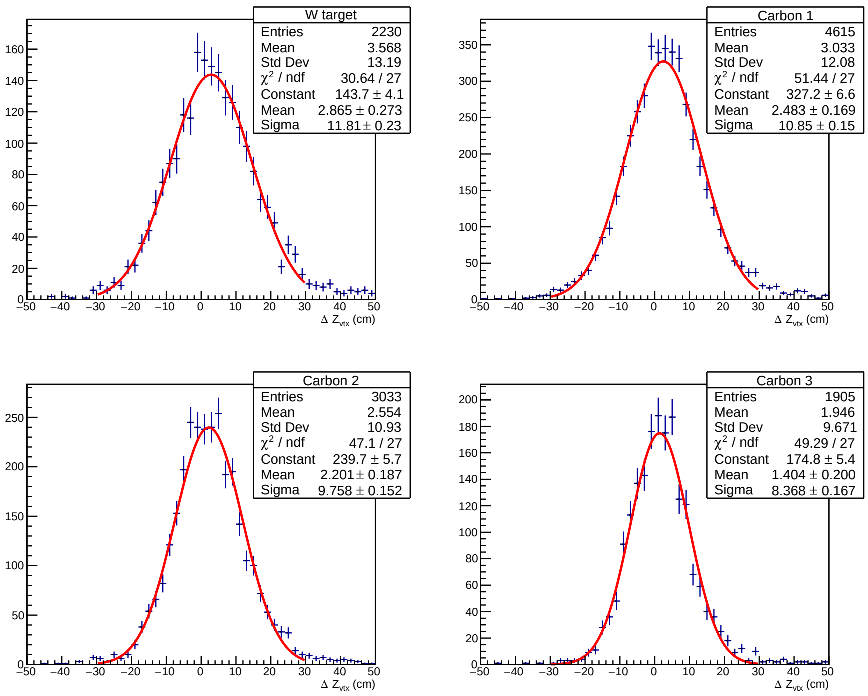

Figure 4.4: Resolution of the primary vertex Z-position for each target for the mass range of $[4, 9]$ GeV/c^2.

Z_{vtx} resolution per target decreases as we move to targets further downstream. This happens because the farther upstream the target is, the smaller the typical angles and the greater the associated error. Without a vertex detector, the typical resolution of the present setup ranges from 11.2 ± 0.2 cm (most upstream) to 8.4 ± 0.2 cm (most downstream), which shows the need for a large spacing between the targets. In fact, these results suggest that more than the current distance of 25 cm between tungsten and carbon is needed to avoid a significant migration of events from one cell to the other. Another fact to be noticed is a reconstruction bias by roughly 2 cm (the reconstructed Z position is systematically downstream of the generated one).

Following the same reasoning, we can calculate $\Delta M_{\mu\mu}$ and Δp_T with:

$$\Delta M_{\mu\mu} = M_{\mu\mu}^{rec} - M_{\mu\mu}^{MC}, \tag{4.3}$$

$$\Delta p_T = p_T^{rec} - p_T^{MC}. \tag{4.4}$$

Table 4.2 presents the results obtained for the different resolutions. For the p_T and $M_{\mu\mu}$ resolutions, the values obtained are similar for each target cell.

	ΔZ_{vtx} (cm)	$\Delta M_{\mu\mu}$ (MeV/c^2)	Δp_T (MeV/c)
W	11.81 ± 0.23	218.9 ± 4.8	134.5 ± 2.6
C1	10.85 ± 0.15	213.6 ± 3.2	132.7 ± 1.2
C2	9.76 ± 0.15	215.1 ± 3.9	135.4 ± 2.2
C3	8.37 ± 0.17	207.3 ± 4.4	151.8 ± 3.1

Table 4.2: Summary of resolutions in Z_{vtx} $M_{\mu\mu}$ and p$_T$ for reconstructed dimuon events for each of the targets.

4.2 Studies on the Optimisation of the Setup

In this section, a vertex detector is introduced at PHAST level. Although these detectors are detailed in the "detectors.dat" file and were used in the simulation of the spectrometer, leading to MC hits generated, they are not included in the CORAL reconstruction (i.e., they were not converted from MC hits to Hits, and their information was not used in the tracks reconstruction). Despite this, we have access to MC information from each reconstructed track, and therefore we can analyse the impact of such detectors on our simulated event reconstruction at PHAST level.

4.2.1 Introduction of the Vertex Detectors

We introduce three generic vertex detector planes into the setup immediately downstream from the carbon target. This hypothetical detector is being considered to improve the Z_{vtx} and dimuon mass resolutions of the AMBER setup.

We start by looking at all the MC hits of the event (i.e., the (x,y) coordinates of the passage of the simulated outgoing charged particles in the active material of the detector). We can access them for each detector and, in this case, for each VD plane. The planes will be referred to as VD1, VD2, and VD3, the first being the most upstream and VD3 the plane closest to the hadron absorber. We will be using the simulation of 150K events done in TGEANT. The next step is to associate the MC hits with the muon tracks. The selection of the MC hits to associate can be done in two ways: try to associate only those MC hits that were created in this plane and belong to the muon MC track (ideal reconstruction), or we can select all the MC hits in this plane, regardless of the MC track that originated them. This step is done differently depending on the studies conducted and is explored in the following subsections. Finally, we want to be able to associate a hit with a reconstructed track. Using a PHAST method, we create a new hit by providing the position (x,y), the associated uncertainties, and the hit time. To calculate the X and Y positions, we want to mimic the behaviour of a pixel/microstrip detector. The position in these detectors is determined by the pixel/strip that the particle crosses. Consequently, the MC hit position was associated with a pixel/strip named bin. The bin centre is then used to create the reconstructed hit. The uncertainty of x and y given to the PHAST method is then determined by the dimension of the pixel. This process is illustrated in Fig. 4.5, where the MC hit position is the red dot, and the hit position used is the centre of the bin it crossed.

One can try associating the reconstructed hit with the reconstructed track using proximity criteria. The method generically used in CORAL and PHAST for track reconstruction is the so-called Kalman filtering,

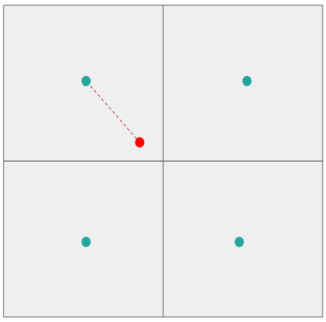

Figure 4.5: Association of MC-hit position with the respective bin.

a complex algorithm of linear quadratic estimation [36], [37]. Once the tracks have been modified, we can proceed to the vertexing process. We select only the updated tracks for which the χ^2_{final}/ndf value does not exceed 10. This extra point(s), closer to the targets and before the muons undergo multiple scattering in the absorber, could provide a more accurate position of the vertex and tracking information, which is the aim of this study.

We consider events where at least one muon crosses one plane of the VDs. The situation of both muons crossing the detector is expected to lead to better resolutions than the one where only one falls in the acceptance of VD, the other passing outside. Therefore, when computing the resolution of each DY variable, there should be two significant contributions, which will be separated when fitting the resolution distributions with a double-Gaussian function. The contribution of each Gaussian to the fit will depend on the number of events with 1 or 2 muons observed. This procedure is what we use in the studies below.

We will now detail each of the detectors considered and the analysis conducted.

4.2.2 Squared Pixel Detector

In PHAST, the hypothetical VD planes (40x40 cm^2) are divided into smaller squares, the pixels. We try different pixel sizes, such as 1×1 cm^2, 1×1 mm^2 and 0.1×0.1 mm^2, to study how the segmentation affects our results on the mass and spatial resolution. For these detectors, we consider the detector resolution as follows [39]:

$$a/\sqrt{12}, \tag{4.5}$$

where a is the size of the pixel.

We start by analysing Table 4.3, which gives the number of particles/muons that hit each VD, obtained by selecting the VD MC hits. One observes that the first plane sees 37 charged particles/event on average. Each event has (at least) two muons generated from Pythia, thus one concludes that only 65428/300000=0.22 of the Drell-Yan muons fall in the geometrical acceptance of this detector to be compared with the 0.58 that are globally in the acceptance of the AMBER spectrometer. It is important to analyse the spatial distribution of all MC hits in the planes, shown in Fig. 4.6. On the other hand, since muons are the particles of interest in our analysis, Fig. 4.7 shows the hit position of DY muons. The Z-axis (colour scale) is different for the

	Z-position (cm)	**MC-hits**	
		All Particles	μ
VD1	-150	5502709	65428
VD2	-127	4654139	65053
VD3	-100	3950182	63359

Table 4.3: Number of MC hits per VD plane for muons and all charged particles.

two cases; however, it is possible to denote in both cases that the highest rate of particles crossing the VDs happens in the central zone. This effect was also observed in the exercise carried out in Geant4 in Fig. 3.5. Combining these figures with the information in Table 4.3, the decrease in the number of particles when we go downstream in the VD planes is justified by the trajectory of the particles. The particles are produced at a given angle, so as we move in the z direction, the distance between the particles' trajectory and the axis is larger. Consequently, the particles are more spread out, and some end up not crossing the last planes.

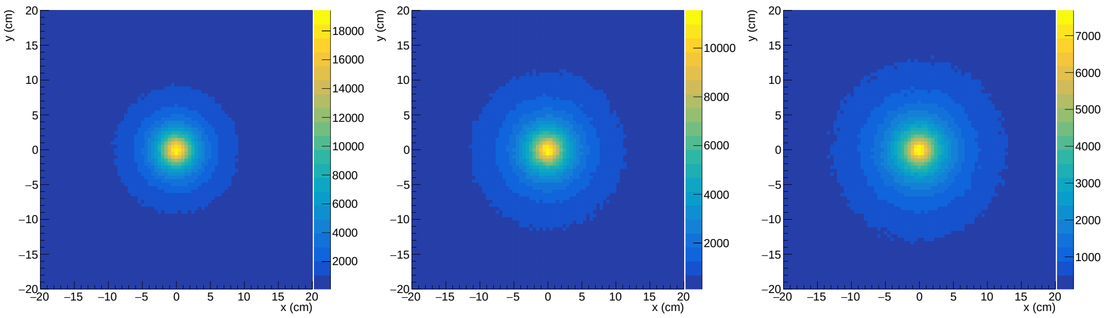

(a) VD1 **(b)** VD2 **(c)** VD3

Figure 4.6: Spatial distribution of MC-hits on the VDs.

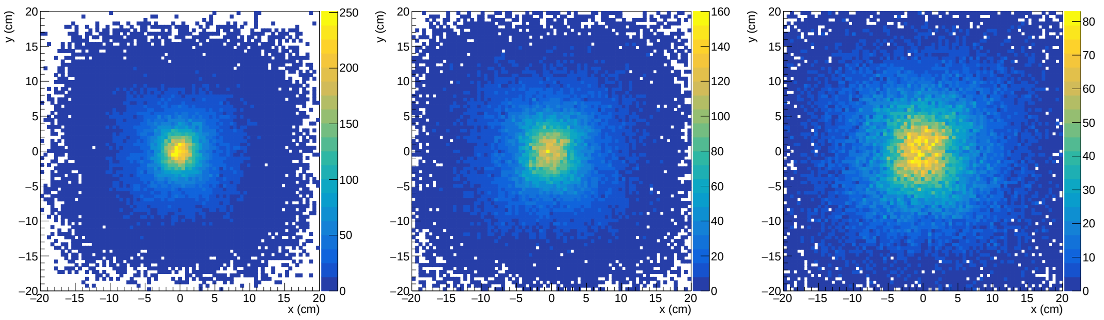

(a) VD1 **(b)** VD2 **(c)** VD3

Figure 4.7: Spatial distribution of the muons MC-hits on the VDs.

Regarding the DY muons, it is interesting to study the events with 0, 1, and 2 muons crossing the VD after the selection cuts, shown in Table 4.4. Almost all the events have both muons crossing the VDs. To further analyse this, Table 4.5 presents the number of VD planes hit by μ^+. Most of these muons cross the three planes.

0 μ	108	0.01
1 μ	162	0.01
2 μ	11513	0.98
total	11783	1.00

Table 4.4: Number of muons that cross the VDs per event.

0	108	0.01
1	75	0.01
2	1033	0.09
3	10562	0.89
total	11783	1.00

Table 4.5: Number of muon hits on the VDs per event.

Squared Pixel detector with ideal reconstruction

In this subsection, we only try to associate the MC hits that we already know were originated from the muon MC track with the reconstructed muon track. We convert its (x,y) coordinates of passage into a bin position and use it to create a new hit posteriorly associated with a reconstructed track. It is an ideal scenario since with real data we do not know which hit is associated with which track. We proceed as explained and add the hits to the tracks.

This exercise mimics a pixel detector using different segmentations, allowing us to see how the pixel size impacts the final results. The detector was divided into 1x1 cm^2, 1x1 mm^2 and 0.1x0.1 mm^2 pixels. In Fig.

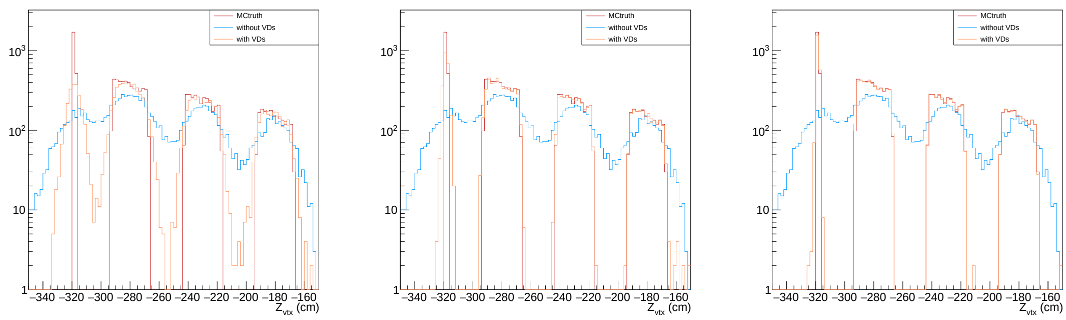

(a) 1 × 1 cm^2 segmentation. **(b)** 1 × 1 mm^2 segmentation. **(c)** 0.1 × 0.1 mm^2 segmentation.

Figure 4.8: Z_{vtx} distribution for MC, reconstructed with and without the VDs events, for different pixel sizes.

4.8, the improvement in the Z-position of the Drell-Yan event vertices, Z_{vtx}, is evident when adding VD hits. The separation of target cells becomes more accentuated, especially tungsten, which was not distinguishable previously.

We analyse the impact of introducing these detectors by looking at two fundamental variables: the dimuon mass and the Z_{vtx} resolutions. The resolution is obtained by the procedure mentioned earlier, where we made a double Gaussian fit to $(Z_{vtx}^{rec} - Z_{vtx}^{MC})$. In this case, $\sim$ 98% of the events will have 2 muons crossing the detectors. The results are mostly simple Gaussians since the events that only had 1 muon will not provide enough statistics to study its resolution distributions. Table 4.6 presents the values obtained for the Z_{vtx} resolution for the different pixel sizes and compares them to the values obtained before introducing the VDs. The Z_{vtx} resolution value shown is from the non-zero Gaussian or the one with the smaller width.

		ΔZ_{vtx} (cm)			
		W	C1	C2	C3
Without VD		11.5 ± 0.2	10.63 ± 0.11	7.386 ± 0.11	7.07 ± 0.44
	1cm	4.447 ± 0.076	3.865 ± 0.047	3.046 ± 0.048	2.413 ± 0.045
Pixel Size	1mm	1.533 ± 0.028	1.232 ± 0.015	0.840 ± 0.013	0.491 ± 0.010
	0.1 mm	0.447 ± 0.011	0.238 ± 0.016	0.219 ± 0.018	0.089 ± 0.003

Table 4.6: Z_{vtx} resolution per target cell for each VD segmentation.

As expected, as we reduce the size of the pixels, the spatial resolution improves, since we can more accurately determine where the particle crossed the VD and get Z_{vtx} closest to the generated. As seen in the previous section, the events that originated in the carbon cell closest to the spectrometer have a better spatial resolution.

Next, we observe the dimuon mass resolution presented in Table 4.7. We also see an improvement in the mass resolution as we have a higher detector segmentation. Compared with the results without the VDs we see a decrease of at least $\sim$ 50 MeV/c^2.

		Δ $M_{\mu\mu}$ (MeV/c^2)			
		W	C1	C2	C3
Without VDs		218.8 ± 4.0	221.8 ± 2.2	217.6 ± 2.7	214.4 ± 3.5
	1cm	173.1 ± 5.0	173.9 ± 2.9	169.0 ± 4.0	163.7 ± 6.5
Pixel Size	1mm	167.1 ± 3.5	154.4 ± 2.1	157.4 ± 3.0	148.5 ± 8.5
	0.1 mm	164.5 ± 4.0	149.5 ± 7.0	128.5 ± 13.6	121.0 ± 12.0

Table 4.7: Dimuon mass resolution per target cell for each VD segmentation.

This reconstruction is ideal, so it does not replicate what would happen to real data. However, it is still important to analyse this case, since this provides the maximal improvement one could expect, to compare with a more realistic case.

Squared pixel detector with realistic hit treatment

In this study, we try to mimic real data track reconstruction, where we have no access to the MC truth. We start with the reconstructed track, whose first measured point is in between the hadron absorber and the SM1 dipole magnet, and we extrapolate it backwards through before the absorber. The PHAST extrapolation method considers multiple scattering and energy loss of muons. As we have access to all the MC hits in the events, we can select the ones for each detector and, in this case, per VD plane. The MC hits are replaced by the corresponding pixel/bin centre position, making it possible to associate the VD hit to the extrapolated track at the VD position using spatial criteria. It is important to highlight that all charged particles in the event will create MC hits when crossing the detector, being of extreme importance to choose adequate criteria to select the good ones (i.e. those that originate from the muons passage).

We begin by calculating the distance between the centre of the active pixel and the muon track extrapolation position, since we are looking for the closest one. However, this criterion is not enough, as we do not want to accept hits 10 cm away from the extrapolated track. We introduce an "uncertainty in the distance" σ_d criterion, calculated using standard error propagation of the track error and the hit error:

$$\sigma_d^2 = \left|\frac{x_{bin} - x_t}{d}\right|^2 (\sigma_{x_t}^2 + \sigma_{x_{bin}}^2) + \left|\frac{y_{bin} - y_t}{d}\right|^2 (\sigma_{y_t}^2 + \sigma_{y_{bin}}^2)\,, \tag{4.6}$$

where d corresponds to the distance, defined as d $= \sqrt{(x_h - x_t)^2 + (y_h - y_t)^2}$. Variables with subscripts t correspond to the extrapolated track parameters. We will then require that the distance between the track and the hit be smaller than $A * \sigma_d$, where the number of sigmas A is a number defined by us. Its purpose is to allow the highest amount of "correct associations", which we can optimise by making use of the MC truth. To do this, we use the MC information and check for every closest hit associated if it belonged indeed to this muon MCtrack. This type of study, i.e. using MC information, is often done to optimise the criteria applied to real data.

We will consider the pixel detector with 1×1 mm^2. It presents good results for the resolutions and is a reasonable solution cost-wise. For the σ_d criterion, we will study the results with 1 σ_d, 3 σ_d, and 6 σ_d. We want to maximise the statistics, but at the same time, we do not want to be adding hits that are 10 cm away, for example. Table 4.8 summarises the results obtained for the σ_d study. "# right $\mu^{\pm}$ hit" corresponds to the number of events where at least one muon hit was chosen correctly according to the MC truth. Table 4.9 mentions the number of events where 1 or 2 muons have hit the VDs for each of the σ_d criteria. As expected, for 1 σ_d the number of events is smaller than for higher sigmas, since for the latter we accept hits farther away from the track, ending up finding one most of the time. This effect is also reflected in the number of muons per event; as we select more hits, the number of events where both muons have associated hits in the VD becomes the majority in the case of 6 σ_d.

		total	**# right μ^+ hit**	**# right μ^- hit**
	1 σ_d	3783	3174	2950
Pixel 1mm	3 σ_d	9097	7802	7174
	6 σ_d	9930	8533	7607

Table 4.8: σ_d study for the hit analysis in the pixel detector.

		total	**events 2μ** (fraction)	**events 1μ** (fraction)
	1 σ_d	3783	323 (0.09)	3460 (0.91)
Pixel 1mm	3 σ_d	9097	3574 (0.39)	5523 (0.61)
	6 σ_d	9930	7658 (0.77)	2272 (0.23)

Table 4.9: Events with 1 or 2 μ in the σ_d study for the hit analysis in the pixel detector.

Fig. 4.9 shows the Z_{vtx} distribution obtained for the events selected with each A*σ_d criterion. Once again, the impact of the introduction of the VD is astounding; the curves are considerably similar to the MC distribution. The distributions obtained for each σ_d follow the same trend. Given these points, we choose the 6 σ_d criterion, maximising the statistics without compromising the quality of the selected hits.

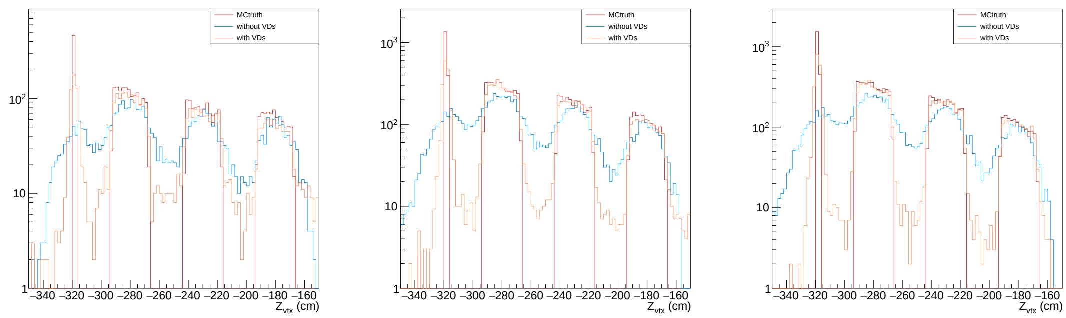

(a) 1 σ_d criterion. **(b)** 3 σ_d criterion. **(c)** 6 σ_d criterion.

Figure 4.9: Z_{vtx} distribution for different σ_d criteria.

After choosing the hit selection criteria, we move on to the results obtained concerning Z_{vtx} and dimuon mass resolutions. Since now we have around one-quarter of the events with 1 μ and around three-quarters with 2 μ crossing the VDs, we will take into account both Gaussians in the double Gaussian fit and analyse the results using both resolutions. Tables 4.10 and 4.11 compare the results obtained in this analysis with the ideal one. It shows small differences between the Z_{vtx} resolutions obtained for the ideal and the hit

		Δ Z_{vtx} (cm)			
		W	C1	C2	C3
2 μ event	Ideal Reconstruction	1.533 ± 0.028	1.232 ± 0.015	0.840 ± 0.013	0.491 ± 0.010
	Realistic Treatment (6 σ_d)	1.346 ± 0.130	1.096 ± 0.038	0.788 ± 0.047	0.463 ± 0.030
1μ events	Realistic Treatment (6 σ_d)	2.252 ± 0.300	2.783 ± 0.462	2.256 ± 1.010	1.509 ± 0.239

Table 4.10: Z_{vtx} resolution obtained for hit analysis in pixel detector.

analysis. When comparing the values with 2 and 1 muons crossing the VDs, as anticipated, we observe a worsening in the resolution obtained. So, even without considering the information from the MC track, we are able to obtain resolutions similar to the ideal reconstruction ones. This is promising and shows the importance of this detector in the future experiment.

		Δ $M_{\mu\mu}$ (MeV/c^2)			
		W	C1	C2	C3
2 μ event	Ideal Reconstruction	167.1 ± 3.5	154.4 ± 2.1	157.4 ± 3.0	148.5 ± 8.5
	Realistic Hit Treatment (6 σ_d)	166.1 ± 9.6	149.8 ± 7.0	160.5 ± 9.9	179.6 ± 17.7
1μ events	Realistic Hit Treatment (6 σ_d)	387.4 ± 365.0	333.0 ± 65.0	349.7 ± 69.7	469.5 ± 363.8

Table 4.11: Dimuon mass resolution obtained for hit analysis in pixel detector.

Table 4.11 shows the values of the calculated dimuon mass resolution. The 1μ events present a considerable worsening of the resolution. The observed values for both resolutions in the realistic treatment have a higher error associated. It results from the two-Gaussian fit, since we do not have a large number of events to fit each target distribution, and sometimes the error obtained is of the order of the resolution itself. Despite this, in the case of the 2μ events, the results obtained are comparable with those of the ideal reconstruction.

4.2.3 FVTX Detector

As a particular case of the vertex detector, we now study the contribution of introducing the already existing FVTX detector, and for this, we need to be able to simulate its geometry. Since the detector included in TGEANT is a silicon plane of 40x40 cm^2, at PHAST level we can segment it as we wish. It is considered a detector with three planes with polar symmetry. It has a hole in the middle with a radius of 4.4 cm and an outer radius of 16.2 cm. It is segmented in the radial direction into 0.0075 cm microstrips and in the ϕ direction into 3.75° slices. Fig. 4.10 illustrates the segmentation of the detector. In this figure, the binning in r is not the same as in the simulation (and in the real detector); otherwise, the bins would not be visible. In this way, the simulated size of each pixel in the radial direction is 0.0075 cm, while in the figure it is $\sim$ 4 mm.

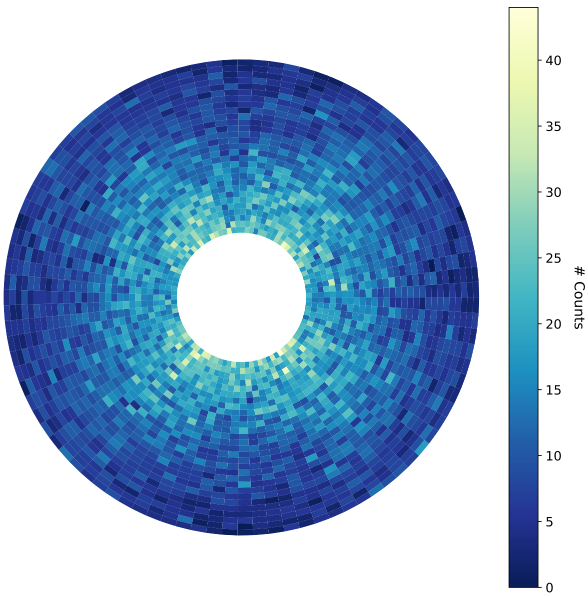

Figure 4.10: FVTX segmentation.

We face a problem in carrying out the analysis for such a detector; PHAST methods are not prepared to handle detectors in polar coordinates. The class that allows us to create a new hit and associate it with a track can only receive as input the values x and y (Cartesian coordinates). For this reason, we need to transform the polar coordinates of the detector into x-y values, using:

$$x = r\cos\phi, \tag{4.7}$$

$$y = r\sin\phi. \tag{4.8}$$

An issue arises from the calculation of the uncertainty associated with each coordinate requested by the PHAST method. The uncertainties in x and y are defined as follows:

$$\sigma_x = \sqrt{(0.0075\cos\phi)^2 + \left(r\sin\phi \times 3.75 \times \frac{\pi}{180}\right)^2} \tag{4.9}$$

$$\sigma_y = \sqrt{(0.0075\sin\phi)^2 + \left(r\cos\phi \times 3.75 \times \frac{\pi}{180}\right)^2} \tag{4.10}$$

These uncertainties are then divided by $\sqrt{12}$ [39]. A downside of the methodology used is that for each bin, depending on the (x,y) position, its uncertainty will differ. Fig. 4.11 shows the graphs for σ_x and σ_y as a function of ϕ, for $r = 8$ cm. We see that the error will be maximum when $\phi = \pi/4$, $\phi = 3\pi/4$,

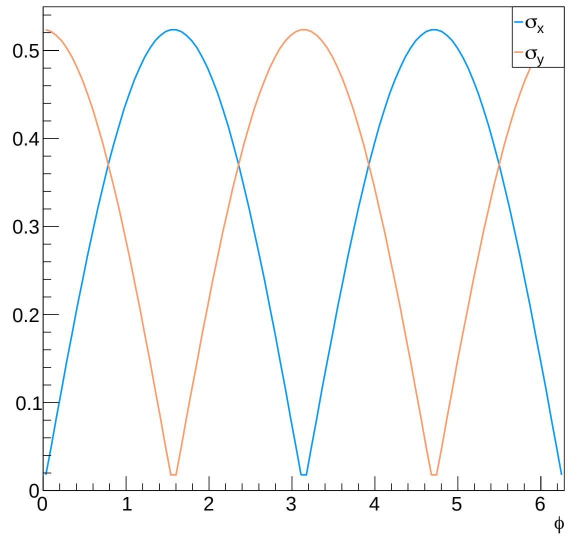

Figure 4.11: x and y uncertainties as a function of ϕ for r=8cm.

$\phi = 5\pi/4$ and $\phi = 7\pi/4$ but this increase associated with the hit uncertainty is artificial since, according to the detector geometry, all the pixels for a given radius are equivalent, the uncertainty being dictated by the pixel size. This method has a significant error overestimation. This error is known and will be overcome once we have a PHAST method to create hits providing polar coordinates as input.

FVTX detector with realistic hit treatment

We start the FVTX study by analysing the MC hits in this detector. We expect different values from the ones obtained for the squared-pixel case since it has different dimensions and a hole in the middle. Table 4.12 shows the number of MC hits per VD plane. The first FVTX plane sees on average 19 charged particles/event, while the squared-pixel detector sees 37. Only 36317/300000=0.12 of the Drell-Yan muons fall in the geometrical acceptance of this detector, which is lower than the 0.22 observed for the squared pixels. Both of the effects are caused by the central hole present in our detector, decreasing the particles' acceptance.

	Z-position (cm)	MC-hits All Particles	μ
VD1	-150	2861922	36317
VD2	-127	2572755	39616
VD3	-100	2242428	40482

Table 4.12: Number of MC hits per VD plane for muons and all charged particles in the FVTX detector.

Realistic Hit Treatment

We follow the same procedure for the FVTX as for the squared pixel detector. We start by choosing a σ_d criterion. Table 4.13 shows how the criteria in the number of σ_d allow association of hits. The table details the number of hits that were correctly associated. Table 4.14 complements this information by showing the number of events with 1 or 2 muons with associated hits in the VDs. We note that as we increase

		total	# right μ^+ hit	# right μ^- hit
	1 σ_d	7462	7004	6720
FVTX	3 σ_d	10726	9614	8893
	6 σ_d	9982	8733	7985

Table 4.13: σ_d study for the hit analysis for the FVTX detector.

		total	events 2μ (fraction)	events 1μ (fraction)
	1 σ_d	7462	1927 (0.26)	5535 (0.74)
FVTX	3 σ_d	10726	6592 (0.61)	4134 (0.39)
	6 σ_d	9982	6757 (0.68)	3225 (0.32)

Table 4.14: Events with 1 or 2 μ in the σ_d study for the hit analysis in the FVTX detector.

our criterion (hence A*σ_d), more events with 2μ hits are accepted. In this case, we have the maximum statistics for 3 σ_d. This σ_d criterion provides greater precision in identifying the right hit, so we will use it. The result differs from those of the squared-pixel detector since we now consider a detector with a hole and with different spatial resolutions for each (x,y) position.

We now proceed to analyse the results obtained, starting with the Z_{vtx} distribution in Fig. 4.12, where the "with VDs" label refers to the case where hit association is performed using the 3 σ_d criterion. The distribution obtained with the FVTX hits shows a good separation between target cells.

In this case, with the 3 σ_d criterion, the selected events contain around 60% of events with two muons and 40% of events with one muon. Therefore, when we perform the double-Gaussian fit we expect to once again see two Gaussians that need to be considered. The fits to the resolution distributions are presented in Appendix A and the obtained Z_{vtx} resolution is shown in Table 4.15, while the dimuon mass resolution is shown in Table 4.16.

The FVTX provides good results for dimuon mass and Z_{vtx} resolution. It is comparable to the results obtained for the 1x1 mm^2 pixel detector. A more detailed discussion of this comparison will be given later

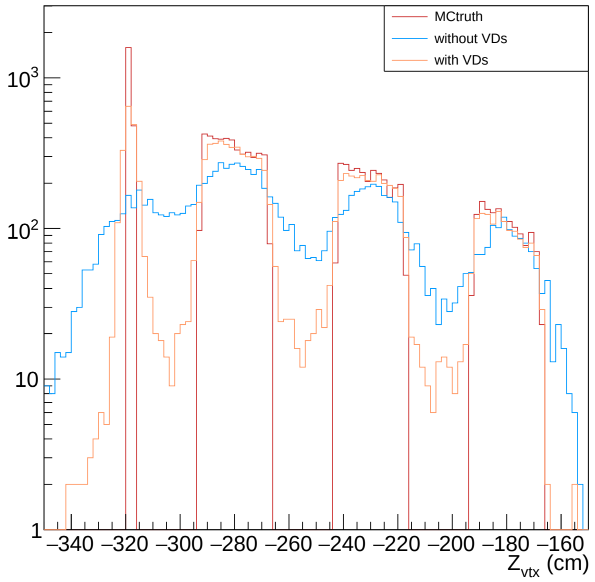

Figure 4.12: Z_{vtx} distribution for the FVTX detector.

		$\Delta\ Z_{vtx}$ (cm)			
		W	C1	C2	C3
2μ events	Pixel 1 x 1 mm^2	1.346 ± 0.130	1.096 ± 0.038	0.788 ± 0.047	0.463 ± 0.030
	FVTX	1.754 ± 0.256	1.354 ± 0.067	0.816 ± 0.048	0.685 ± 0.084
1μ events	Pixel 1 x 1 mm^2	2.252 ± 0.300	2.783 ± 0.462	2.256 ± 1.010	1.509 ± 0.239
	FVTX	3.404 ± 0.896	3.781 ± 0.290	2.142 ± 0.131	1.595 ± 0.276

Table 4.15: Z_{vtx} resolution obtained for hit analysis in pixel detector.

		Δ M$_{\mu\mu}$ (MeV/c^2)			
		W	C1	C2	C3
2μ events	Pixel 1x1 mm^2	166.1 ± 9.6	149.8 ± 7.0	160.5 ± 9.9	179.6 ± 17.7
	FVTX	152.2 ± 15.1	156.9 ± 13.9	137.2 ± 19.8	102.6 ± 20.2
1μ events	Pixel 1x1 mm^2	387.4 ± 365.0	333.0 ± 65.0	349.7 ± 69.7	469.5 ± 363.8
	FVTX	237.4 ± 31.3	401.2 ± 363.3	285.2 ± 102.0	205.7 ± 102.0

Table 4.16: Dimuon mass resolution obtained for hit analysis in pixel detector.

in Section 4.2.4. As for the comparison between the 1 μ and 2 μ events, as expected, we observe a worse spatial resolution (for all targets) for the events in which only one muon crosses the VD. But even for these cases, the resolution obtained is low compared to the situation where we have no VDs. This tendency is also noted in the dimuon mass resolution. The dimuon mass resolution for 2μ events presents an improvement compared to the 1x1 mm^2 pixel detector. These results need to be interpreted with caution due to the overestimation of the uncertainties of x and y for this detector.

Study on the impact of detectors position

An additional study is done to study the sensitivity to the positions of the VD planes and the distance between the planes. It required running the TGEANT simulation again while changing the VD planes' position. They were moved from -150, -127 and -100 cm to -110, -103.97 and -97.94 cm as closely as possible from the hadron absorber. The distance between the planes mimics the distance between the real FVTX planes ($\sim$ 6 cm). For this study, we generated 49K events.

With the VDs in different positions, we expect the number of particles that cross them to be different, as well as the spatial distribution of the hits. Table 4.17 presents the number of particles/muons that hit the VD planes. When comparing them with those for the VDs in the previous layout in Table 4.3 we confirm that the values differ considerably. We need to consider that this generation was done with around 1/3 of

		MC-hits	
	Z-position (cm)	All Particles	μ
VD1	-110	763994	13415
VD2	-103.97	742405	13491
VD3	-97.94	722260	13445

Table 4.17: Number of MC hits per VD plane for muons and all particles, for the new VD positions.

the statistics. Therefore, we take into account the number of DY muons (we have at least 2 muons) and the number of charged particles per event. Table 4.18 summarises the values obtained for this calculation and compares them with those of the previous VD setup. We see a reduction in the number of particles that

	Particles per event			
	New Layout		Previous Layout	
	All particles	μ	All particles	μ
VD1	15.59	0.14	19.08	0.12
VD2	15.15	0.14	17.15	0.13
VD3	14.74	0.14	14.95	0.13

Table 4.18: Comparison between the fraction of particles MC hits per generated event in the new and the previous layout.

hit the first plane when comparing the two analyses, as expected because the planes are farther downstream now. However, this does not reflect on the fraction of DY muons per event, since it even increases from 0.13 to 0.14. It reveals that even when the first plane is moved almost 40 cm from the target, the muon angular acceptance does not decrease but there is a reduction in the fraction of other particles reaching the detector, which is positive. The fraction of particles in VD2 and VD3 is similar to that of VD3 in the previous analysis because they are placed at a similar Z (around 100 cm). Moreover, the decrease of particle hits observed as we go downstream in the VD planes is smaller, as the planes are now closer together.

We perform the VD analysis to obtain results closest to what we would get in the future experiment. We select the σ_d criterion as 3 σ_d, as it was chosen for the previous FVTX analysis. The number of events obtained after the analysis steps is provided in Table 4.19. We have 2 muons crossing the VDs in half of the events, which means that both Gaussians will be of relevance in the double gaussian fit.

total	**events 2μ** (fraction)	**events 1μ** (fraction)
3488	1793 (0.51)	1695 (0.49)

Table 4.19: Number of reconstructed events for the new FVTX layout.

Fig. 4.13 presents the Z_{vtx} distribution obtained for the simulated conditions, in which target separation is evident.

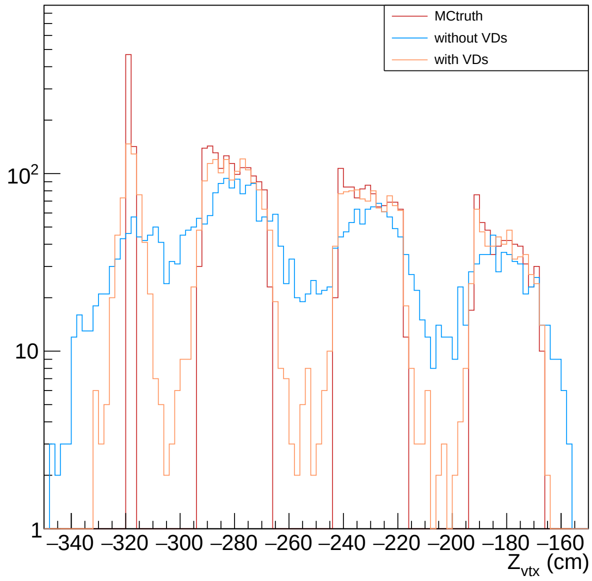

Figure 4.13: Z_{vtx} distribution for the new layout of FVTX detector.

Table 4.20 shows a comparison between the Z_{vtx} resolution of this FVTX layout and the previous one for events where 2 and 1 muons cross the VDs. The fits performed to obtain these results are presented in Appendix A. The vertex resolution tends to be worse for the targets farther upstream, so it is expected that as we move the VDs downstream the resolution worsens.

		Δ Z_{vtx} (cm)			
		W	C1	C2	C3
2 μ event	FVTX previous layout	1.754 $\pm$ 0.256	1.354 $\pm$ 0.067	0.816 $\pm$ 0.048	0.685 $\pm$ 0.084
	FVTX new layout	2.421 $\pm$ 0.189	1.704 $\pm$ 0.434	1.319 $\pm$ 0.864	0.744 $\pm$ 0.176
1 μ event	FVTX previous layout	3.404 $\pm$ 0.896	3.781 $\pm$ 0.290	2.142 $\pm$ 0.131	1.595 $\pm$ 0.276
	FVTX new layout	3.801 $\pm$ 1.414	3.212 $\pm$ 0.648	2.348 $\pm$ 3.168	1.718 $\pm$ 0.224

Table 4.20: Z_{vtx} resolution obtained for the hit analysis in the previous and new FVTX layout.

The difference in Z_{vtx} resolution is between 0.5 and 1 cm, depending on the target. However, the values obtained offer still a great improvement compared to the situation without VDs.

The layout change shows a greater impact on the dimuon mass resolution, as summarised in Table 4.21. The new FVTX layout provides an improvement on the dimuon mass resolution, seen in both events with 2

		Δ $M_{\mu\mu}$ (MeV/c^2)			
		W	C1	C2	C3
2μ events	FVTX previous layout	152.2 $\pm$ 15.1	156.9 $\pm$ 13.9	137.2 $\pm$ 19.8	102.6 $\pm$ 20.2
	FVTX new layout	137.8 $\pm$ 41.1	110.2 $\pm$ 19.0	133.6 $\pm$ 16.9	79.9 $\pm$ 56.4
1μ events	FVTX previous layout	237.4 $\pm$ 31.3	401.2 $\pm$ 363.3	285.2 $\pm$ 102.0	205.7 $\pm$ 10.2
	FVTX new layout	199.6 $\pm$ 26.9	252.1 $\pm$ 50.7	266.5 $\pm$ 51.3	204.8 $\pm$ 38.4

Table 4.21: Dimuon mass resolution obtained for the hit analysis in the previous and new FVTX layouts.

and 1 muon crossing the VDs. The results need to be considered carefully, since due to the low amount of statistics available, the values obtained present a large uncertainty associated.

4.2.4 Discussion

In the previous subsection, we performed several analyses to test how the characteristics of the different detectors affect the results obtained. We tested distinct VD segmentations, geometries, and positions. The results obtained for each target cell are shown. The remarkable impact that such a detector would have on our experiment is evident. For the Z_{vtx} distribution, the separation of the target cells becomes significantly more evident and the distributions become much closer to the MC distribution. This is reflected in the Z_{vtx} resolution, where the observed values for all cases are much lower than those of when VDs were not considered. As the Z_{vtx} resolution becomes much lower than the cell separation, one could safely consider decreasing the distance between cells, namely for the 3 carbon ones, where event migration between cells does not endanger the interpretation of physics results. The reduction of this spacing would allow the whole set of targets to move closer to the absorber, in principle increasing global acceptance. The resolution improvement for the tungsten greatly impacts the purity of the reconstructed samples, and this is essential when studying the nuclear effects of Drell-Yan events. Regarding the dimuon mass resolution, there is an improvement, although the impact is not as large as that in the Z_{vtx} resolution. We were unable to achieve values as good as those presented in the AMBER proposal [17] for the carbon targets ($\sim$ 110 MeV/c^2) for all the cases studied, but the results with the new FVTX layout (more realistic) present values compatible with those in the proposal. In our analysis, by looking at each target, we see that the tungsten one presents the worst spatial and mass resolutions in all cases. This is a consequence of it being the furthest away from the spectrometer and of being a very heavy material (the DY muons suffer much larger multiple scattering when crossing it than for the carbon case), resulting in worse track reconstruction.

We performed an analysis of the segmentation of the pixel detector using the MC truth (a biased selection of MChits to associate with the tracks). It was clear that as we decreased the size of the pixels, better results were obtained, especially for the Z_{vtx} resolution. It represents the maximal improvement one could expect and hence is not realistic. Consequently, we can infer that 0.1 x 0.1 mm^2 is the preferred pixel size. However, we should not take these resolution values as realistic. In the future experiment, at the proposed beam intensity of 100 million beam particles per second, we will have events pile up, which was not considered in these simulations. Time cuts will help reduce part of the uncorrelated hits, but it will nevertheless be a more challenging situation in terms of the illumination of the detectors than the one simulated here, and this is expected to degrade the resolutions.

Subsequently, an analysis was done using a realistic hit treatment. We started by considering the 1x1 mm^2 pixel size. The introduction of new detectors depends on two main things: the available budget and the impact that the detector would have on data collection. There should be a compromise between them. In this case, as we decrease the pixel size, we increase the number of pixels to cover the same area, and the read-out electronics become more complicated and expensive. In further studies, we decided to proceed with the 1x1 mm^2 pixels, since it should be a good option in terms of cost while providing mass resolutions that are not far from those with the smallest pixel size considered. On the other hand, the Z_{vtx} resolution seems sufficient to meet the requirement of properly separating the two target materials. With this, we selected the appropriate criterion $A * \sigma_d$ for which we accepted the MC hits and calculated the Z_{vtx} and the dimuon mass resolution. Comparing the results with those of the ideal reconstruction confirms that the values obtained are slightly better. With this analysis, for the tungsten target and considering 2μ events, we obtained $\Delta M_{\mu\mu} = 166.1 \pm 9.6$ MeV/c^2 and $\Delta Z_{vtx} = 1.346 \pm 0.130$ cm. For the second carbon target, we get Δ $M_{\mu\mu} = 160.5 \pm 9.9$ MeV/c^2 and ΔZ_{vtx} =0.788 $\pm$ 0.047 cm. The improvement in the results obtained in the realistic hit treatment can be the result of the separation of 2μ and 1μ events while performing the double Gaussian fit. The wider Gaussian, the one associated with the 1μ can consider other contributions that would worsen the resolution (events where not all the hits were correctly associated, events with a muon only crossing one plane, etc.).

The next study was done using the FVTX detector, with a different pixel segmentation and a central dead zone. We observed that the number of charged particles and DY muon hits in the first plane decreases, due to the hole in the central zone of the planes and to the smaller active area of the FVTX as compared to the squared pixels VD (836 cm^2 versus 1600 cm^2). We carried out the realistic hit treatment study, but due to a limitation in the presently available PHAST methods, there is an overestimation in the calculated x-y uncertainties. The results obtained for the Z_{vtx} resolutions tend to be worse than those for the squared-pixel detector ones, which is justified by the larger pixel size in FVTX. Even with this, the values obtained show a notorious improvement when compared to the situation without VDs. Regarding the dimuon mass resolution, the values obtained are comparable with those in the squared pixel detectors, and for some targets even better. We obtain for events where 2μ cross the VDs Δ $M_{\mu\mu} = 152.2 \pm 15.1$ MeV/c^2 and $\Delta Z_{vtx} = 1.754 \pm 0.256$ cm for the target tungsten. For the second carbon target, we get Δ $M_{\mu\mu} = 137.2 \pm 19.8$ MeV/c^2 and $\Delta Z_{vtx} = 0.816 \pm 0.048$ cm. The results obtained for FVTX present higher uncertainty, as there were fewer statistics to fit the 2μ events.

In the first simulation with the FVTX geometry, we did not use the actual distance between the planes ($\sim$ 6 cm). So, in the following study, we ran the Monte-Carlo simulation chain starting with TGEANT with the detectors in -110, -103.97, and -97.94 cm (i.e., having a more realistic interplane distance). We generated fewer events, $\sim$ 49k, and did the same analysis as before. As expected, the number of particles that reach the detector is smaller than before because we are farther away from the targets. However, there is no decrease in the number of DY muons, which means that placing the FVTX set at the closest possible position from the absorber is optimal for not losing in terms of muon acceptance. The Z_{vtx} resolution becomes worse than before because there are now relatively more cases in which only one of the muons in the event crosses the VDs. While for the dimuon mass resolution, we observe an improvement to that of the previous layout. We obtained $\Delta M_{\mu\mu}$ = 137.8 ± 41.1 MeV/c^2 and ΔZ_{vtx} = 2.421 ± 0.189 cm, for the tungsten target. For the second carbon target, we got $\Delta M_{\mu\mu}$ = 133.6 ± 16.9 MeV/c^2 and ΔZ_{vtx} = 1.319 ± 0.864 cm. These results were obtained with one third of the events of the previous layout, thus the higher errors associated with the values obtained.

As mentioned before, the placement of the VDs before the hadron absorber presents a challenge. The detector is crossed by an extremely high rate of particles, which may saturate and eventually damage the detector. A preliminary study on this matter was done in Geant4 (in subsection 3.2.1) and, as shown, the presence of a central dead zone avoids this problem. In the case of FVTX, the detector already presents a hole of fixed dimension. Although the size of the hole was not optimised for our beam energy/experimental setup, we can adjust the detector's position between the absorber and the targets to maximise the statistics.

All of these studies point to the advantages and disadvantages of each type of detector. The squared pixel detector guarantees the best Z_{vtx} results for the 1x1 mm^2 pixel. Even for this size, the costs of such a detector are high, considering the electronics, the materials and also the introduction of another detector for time reference (mentioned in section 2.2). This detector does not exist yet, and the DY programme is planned to start in 2025, so there are also time constraints. FVTX is an affordable option, but it has its drawbacks. The spatial resolution provided is worse than the squared-pixel one. It has fixed dimensions, including the pixel size, the inner and outer radius, the plane distance, etc, which are not necessarily the best for the DY programme and lead to a decrease in the muons' angular acceptance, which can be tackled by choosing a Z position closer to the absorber as seen. Nevertheless, the FVTX seems presently the most solid option. It already exists and, given the time and money restrictions, it appears to be the best alternative.

In the future, when there is a PHAST method that can define new hits in polar coordinates, the analysis should be repeated to obtain more accurate results for this setup.

Chapter 5

Conclusions

In this work, pion-induced DY simulations were carried out for a possible AMBER DY setup, with the aim of studying the impact of introducing a dedicated vertex detection system.

In Chapter 1, the Drell-Yan process is described. This process has been studied experimentally throughout the years as a way to gain privileged access to the dynamics inside the colliding hadrons. Thus, a pion-induced Drell-Yall is the most direct way to access information on the pion structure, allowing us to study the pion PDFs.

In Chapter 2, the AMBER experiment is introduced as a future fixed-target experiment located at the M2 beam line at CERN and that proposes to measure, in a first phase, pion-induced DY using both beam charges at 190 GeV/c, for the DY programme. The proposed AMBER DY setup would allow us to do valence and sea separation of the pion PDFs and also study nuclear effects, by introducing a carbon and tungsten target. The introduction of vertex detectors in the target region is being studied to improve muon tracking and, thus, improve the vertex position resolution.

The AMBER Monte Carlo simulation chain is explained in Chapter 3 and was used to simulate a possible DY setup for the future experiment. The software packages used were PYTHIA 8, a general-purpose physics generator; followed by TGEANT which includes a detailed description of the spectrometer and simulates the passage of particles through it, returning the response of the detectors; CORAL to reconstruct the data obtained from TGEANT, and finally, PHAST that is used to analyse the data and access both simulated truth and the reconstructed information. At the end of the chapter, the typical DY kinematic distributions are studied. A more detailed analysis was performed to obtain the geometrical and global acceptance and resolution of several DY distributions. For the DY dimuon, we obtained a geometrical acceptance of 36.9 ± 0.2 % and a reconstruction efficiency of 75.6 ± 0.5 %. Regarding the resolution studies, without the vertex detector, the dimuon mass resolution was around 200 MeV/c^2, while the Z_{vtx} resolution was around 10 cm.

Chapter 4 begins with a more detailed study of the acceptances and resolutions obtained for the DY kinematic distributions. It is followed by the optimisation study on the introduction of vertex detectors. Different VD segmentations, geometries, and positions were tested. The impact of different pixel sizes for a squared-pixel detector was studied and compared with that of FVTX, which presents a different geometry.

Finally, the positions of the VD planes and the distance between the planes were changed to test how it would impact the results from FVTX. The distributions obtained in all studies show the remarkable impact that such a detector would have in our experiment, especially for the Z_{vtx} distribution. From this study, it was concluded that FVTX seems to present the most solid option. We obtained Δ $M_{\mu\mu}$ = 152.2 $\pm$ 15.1 MeV/c^2 and ΔZ_{vtx} = 1.754 $\pm$ 0.256 cm for the target tungsten. For the second carbon target, we get Δ $M_{\mu\mu}$ = 137.2 $\pm$ 19.8 MeV/c^2 and ΔZ_{vtx} = 0.816 $\pm$ 0.048 cm The values obtained show a notorious improvement compared to the situation without VDs.

Part of future work is to add this detector to CORAL's reconstruction process. This includes a detailed description of the detector geometry, which is particularly challenging for the case of FVTX, since CORAL is mostly used for wire detectors.

In the simulations used for this work, only a Drell-Yan interaction was generated per event. A more realistic approach, with the introduction of pile-up, can be studied. This would be a next step of extreme importance to take into account the high rate of particles that reach the detector with such a high beam intensity. Other improvements could include simulating the 4 planes of the FVTX instead of just 3; optimally extending the tungsten beam plug; including more detectors for precise beam reconstruction in the beam telescope; and including a SAS-SAS dimuon trigger, which will be possible in AMBER.

Bibliography

[1] J. Christenson *et al.*, "Observation of massive muon pairs in hadron collisions", *Physical Review Letters*, vol. 25, no. 21, p. 1523, 1970.

[2] S. D. Drell and T.-M. Yan, "Massive Lepton Pair Production in Hadron-Hadron Collisions at High-Energies", *Phys. Rev. Lett.*, vol. 25, pp. 316–320, 1970.

[3] M. Aghasyan et al., "First measurement of transverse-spin-dependent azimuthal asymmetries in the drell-yan process", *Phys. Rev. Lett.*, vol. 119, p. 112 002, 11 2017.

[4] G. Altarelli, R. K. Ellis, and G. Martinelli, "Large Perturbative Corrections to the Drell-Yan Process in QCD", *Nucl. Phys. B*, vol. 157, pp. 461–497, 1979.

[5] G. Parisi, "Summing Large Perturbative Corrections in QCD", *Phys. Lett. B*, vol. 90, pp. 295–296, 1980.

[6] M. Abreu *et al.*, "Anomalous j suppression in pbpb interactions at 158 gev/c per nucleon", *Physics Letters B*, vol. 410, no. 2, pp. 337–343, 1997.

[7] S. Bailey, T. Cridge, L. A. Harland-Lang, A. D. Martin, and R. S. Thorne, "Parton distributions from LHC,HERA,tevatron and fixed target data: MSHT20 PDFs", *The European Physical Journal C*, vol. 81, no. 4, Apr. 2021.

[8] J. Badier *et al.*, "Experimental determination of the π meson structure functions by the drell-yan mechanism", *Zeitschrift für Physik C Particles and Fields*, vol. 18, no. 4, pp. 281–287, 1983.

[9] B. Betev *et al.*, "Observation of anomalous scaling violation in muon pair production by 194 gev/c π–tungsten interactions", *Zeitschrift für Physik C Particles and Fields*, vol. 28, no. 1, pp. 15–22, 1985.

[10] J. Conway *et al.*, "Experimental study of muon pairs produced by 252-gev pions on tungsten", *Physical Review D*, vol. 39, no. 1, p. 92, 1989.

[11] M. Bonesini *et al.*, "High transverse momentum prompt photon production by π- and π+ on protons at 280 gev/c", *Zeitschrift für Physik C Particles and Fields*, vol. 37, no. 4, pp. 535–544, 1988.

[12] C. De Marzo *et al.*, "A Measurement of Direct Photon Production at Large Transverse Momentum in $\pi^- p$, $\pi^+ p$ and pp Collisions at 300-GeV/c", *Phys. Rev. D*, vol. 36, p. 8, 1987.

[13] P. J. Sutton, A. D. Martin, R. G. Roberts, and W. J. Stirling, "Parton distributions for the pion extracted from Drell-Yan and prompt photon experiments", *Phys. Rev. D*, vol. 45, pp. 2349–2359, 1992.

[14] M. Gluck, E. Reya, and A. Vogt, "Pionic parton distributions", *Z. Phys. C*, vol. 53, pp. 651–656, 1992.

[15] M. Glück, E. Reya, and I. Schienbein, "Pionic parton distributions revisited", *The European Physical Journal C*, vol. 10, no. 2, pp. 313–317, 1999.

[16] P. C. Barry, N. Sato, W. Melnitchouk, and C.-R. Ji, "First monte carlo global qcd analysis of pion parton distributions", *Phys. Rev. Lett.*, vol. 121, p. 152 001, 15 Oct. 2018.

[17] B. Adams et al., "COMPASS++/AMBER: Proposal for Measurements at the M2 beam line of the CERN SPS Phase-1: 2022-2024", *CERN-SPSC-2019-022 (SPSC-P-360)*, 2019.

[18] A. S. Ito *et al.*, "Measurement of the continuum of dimuons produced in high-energy proton-nucleus collisions", *Phys. Rev. D*, vol. 23, pp. 604–633, 3 Feb. 1981.

[19] J. Badier *et al.*, "Experimental Determination of the pi Meson Structure Functions by the Drell-Yan Mechanism", *Z. Phys. C*, vol. 18, p. 281, 1983.

[20] K. J. Anderson *et al.*, "Production of Muon Pairs by 225-GeV pi+-, K+, p+- Beams on Nuclear Targets", *Phys. Rev. Lett.*, vol. 42, p. 944, 1979.

[21] D. M. Kaplan *et al.*, "Study of the high-mass dimuon continuum in 400-gev proton-nucleus collisions", *Phys. Rev. Lett.*, vol. 40, pp. 435–438, 7 Feb. 1978.

[22] J. Aubert *et al.*, "The ratio of the nucleon structure functions f2n for iron and deuterium", *Physics Letters B*, vol. 123, no. 3, pp. 275–278, 1983.

[23] J. W. Cronin *et al.*, "Production of hadrons at large transverse momentum at 200, 300, and 400 gev", *Phys. Rev. D*, vol. 11, pp. 3105–3123, 11 Jun. 1975.

[24] P. Abbon *et al.*, "The compass experiment at cern", *Nuclear Instruments and Methods in Physics Research Section A: Accelerators, Spectrometers, Detectors and Associated Equipment*, vol. 577, no. 3, pp. 455–518, 2007.

[25] P. Abbon *et al.*, "The compass setup for physics with hadron beams", *Nuclear Instruments and Methods in Physics Research Section A: Accelerators, Spectrometers, Detectors and Associated Equipment*, vol. 779, pp. 69–115, 2015.

[26] M. Mager et al., "Alpide, the monolithic active pixel sensor for the alice its upgrade", *Nuclear Instruments and Methods in Physics Research Section A Accelerators Spectrometers Detectors and Associated Equipment*, vol. 824, pp. 434–438, 2016.

[27] C. Aidala *et al.*, "The phenix forward silicon vertex detector", *Nuclear Instruments and Methods in Physics Research Section A: Accelerators, Spectrometers, Detectors and Associated Equipment*, vol. 755, pp. 44–61, 2014.

[28] T. Sjöstrand *et al.*, "An introduction to pythia 8.2", *Computer physics communications*, vol. 191, pp. 159–177, 2015.

[29] "Tgeant",

[30] T. Szameitat, "New geant4-based monte carlo software for the compass-ii experiment at cern", Ph.D. dissertation, Jan. 2017.

[31] S. Agostinelli et al., "Geant4—a simulation toolkit", *GEANT4: A Simulation toolkit, Nucl. Instrum. Meth.*, vol. A506, no. 3, pp. 250–303, 2003.

[32] "Coral",

[33] "Physics analysis software tools of compass",

[34] A. Buckley *et al.*, "LHAPDF6: Parton density access in the LHC precision era", *The European Physical Journal C*, vol. 75, no. 3, Mar. 2015.

[35] R. L. Workman *et al.*, "Review of Particle Physics", *PTEP*, vol. 2022, p. 083C01, 2022.

[36] R. Frühwirth, P. Kubinec, W. Mitaroff, and M. Regler, "Vertex reconstruction and track bundling at the lep collider using robust algorithms", *Computer Physics Communications*, vol. 96, no. 2, pp. 189–208, 1996.

[37] P. Billoir, R. Frühwirth, and M. Regler, "Track element merging strategy and vertex fitting in complex modular detectors", *Nuclear Instruments and Methods in Physics Research Section A: Accelerators, Spectrometers, Detectors and Associated Equipment*, vol. 241, no. 1, pp. 115–131, 1985.

[38] R. Brun and F. Rademakers, "ROOT: An object oriented data analysis framework", *Nucl. Instrum. Meth. A*, vol. 389, pp. 81–86, 1997.

[39] H. Spieler, *Semiconductor Detector Systems*. Oxford University Press, Aug. 2005.

Appendix A

Optimization Studies

A.1 Squared Pixel Detector - Realistic Hit Treatment

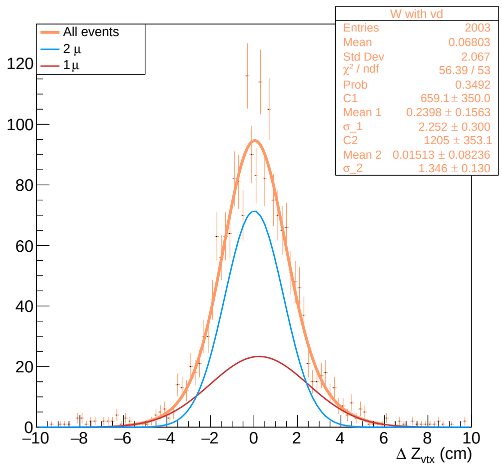

(a) W cell.

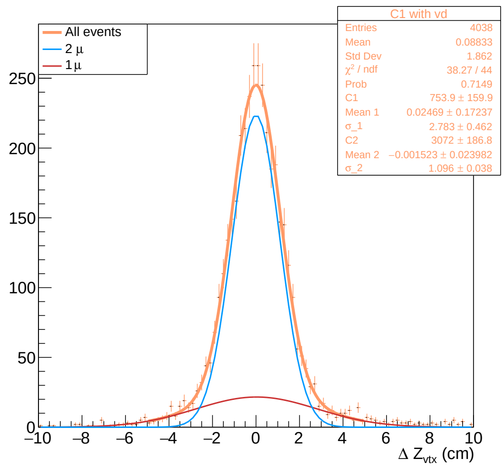

(b) C1 cell.

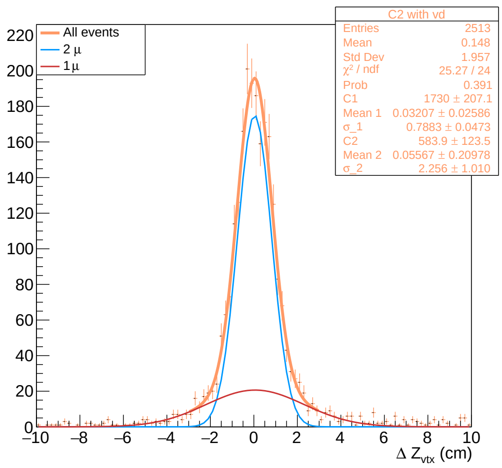

(c) C2 cell.

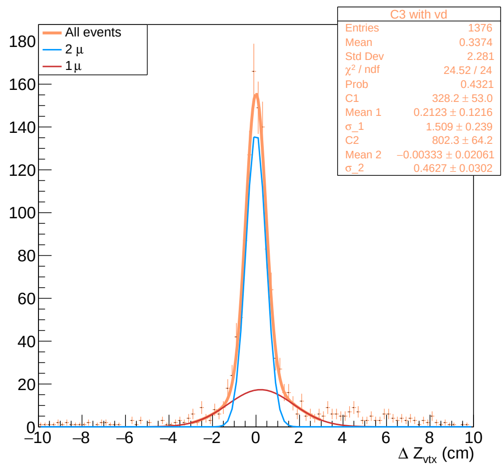

(d) C3 cell.

Figure A.1: Z_{vtx} resolution for the realistic hit treatment, considering a squared pixel detector.

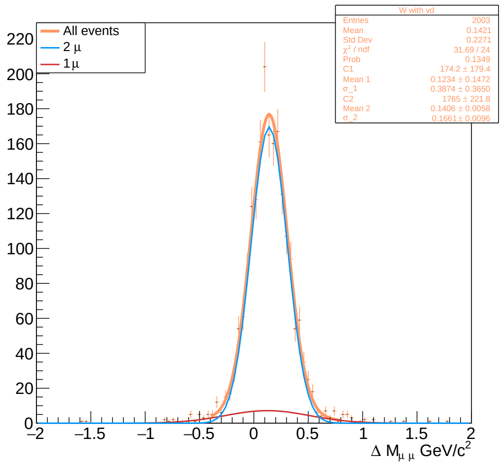

(a) W cell.

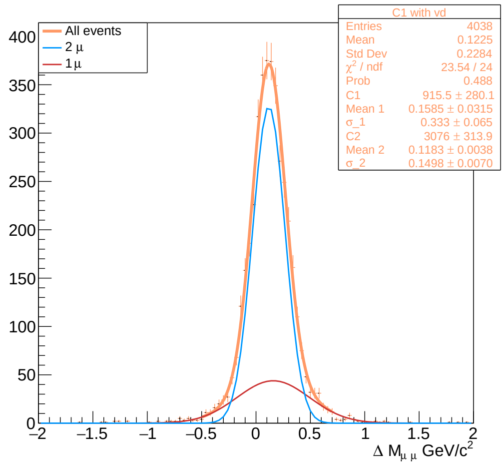

(b) C1 cell.

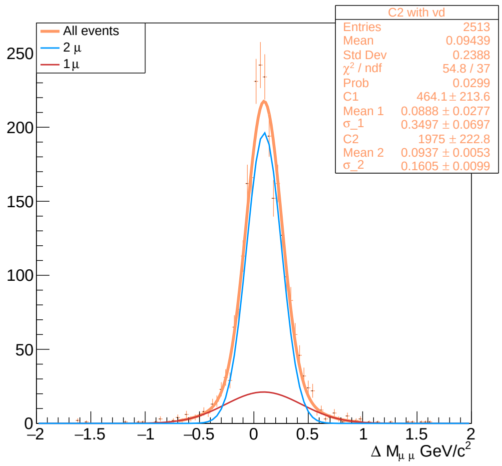

(c) C2 cell.

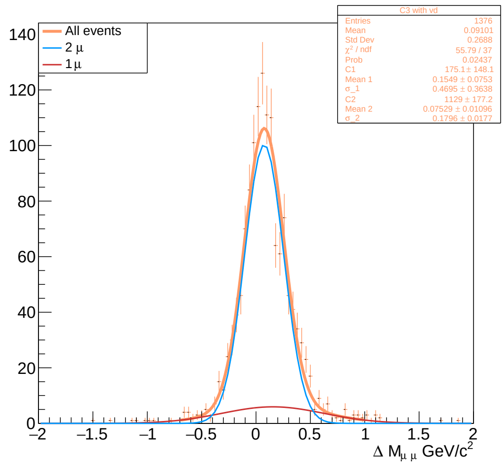

(d) C3 cell.

Figure A.2: Dimuon mass resolution for the realistic hit treatment, considering a squared pixel detector.

A.2 FVTX Detector (first layout)- Realistic Hit Treatment

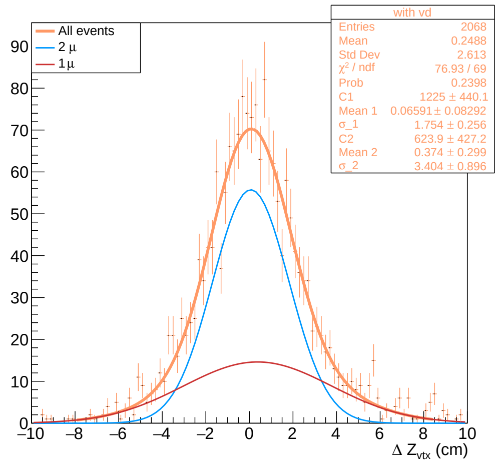

(a) W cell.

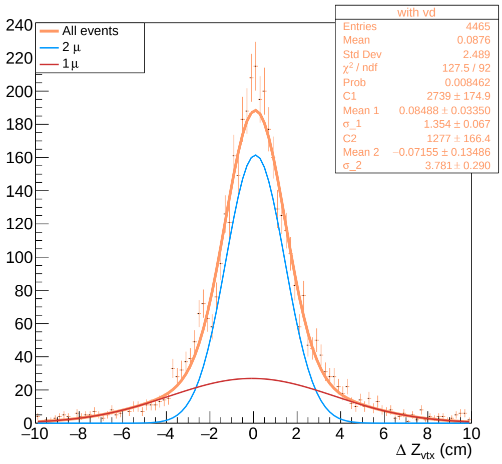

(b) C1 cell.

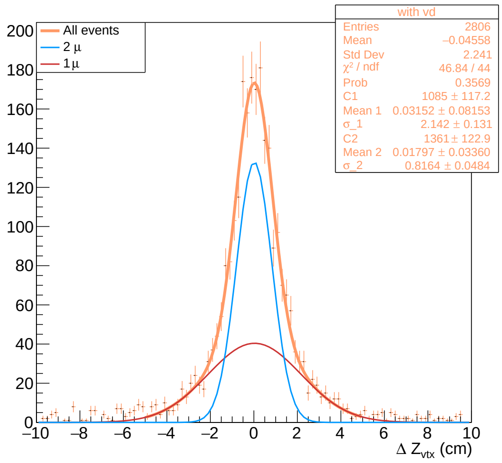

(c) C2 cell.

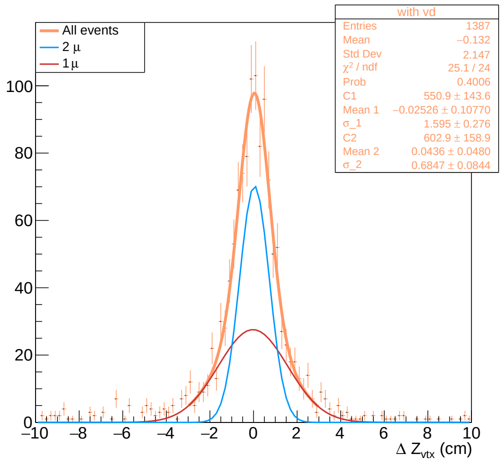

(d) C3 cell.

Figure A.3: Z_{vtx} Resolution for the realistic hit treatment, considering the FVTX detector.

A.3 FVTX Detector (new layout)- Realistic Hit Treatment

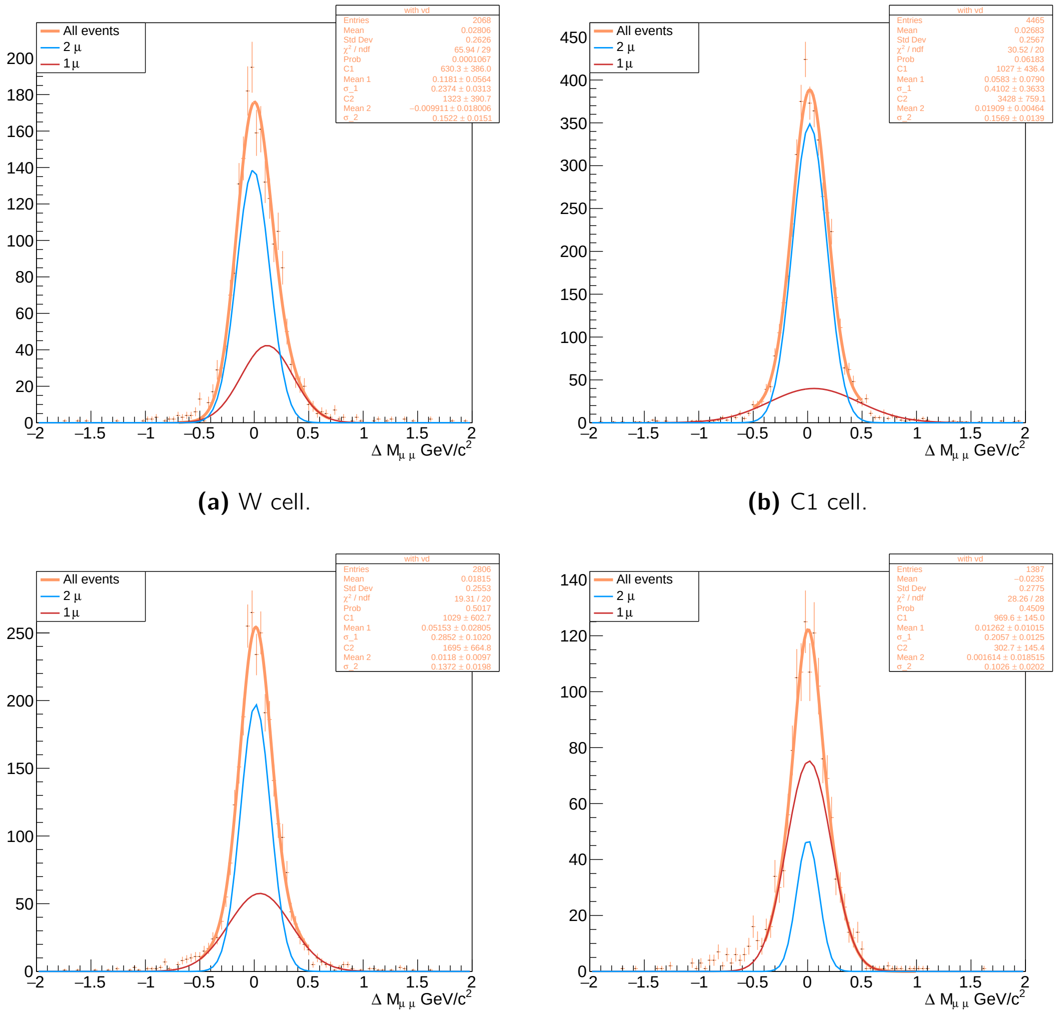

(a) W cell.

(b) C1 cell.

(c) C2 cell.

(d) C3 cell.

Figure A.4: Dimuon mass resolution for the realistic hit treatment, considering the FVTX detector.

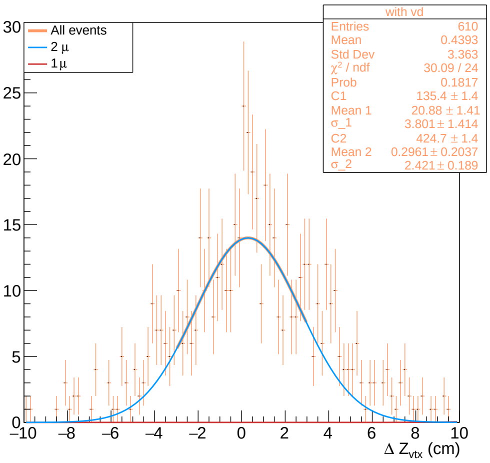

(a) W cell.

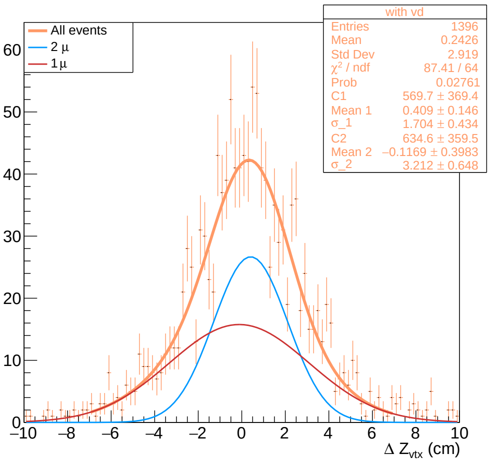

(b) C1 cell.

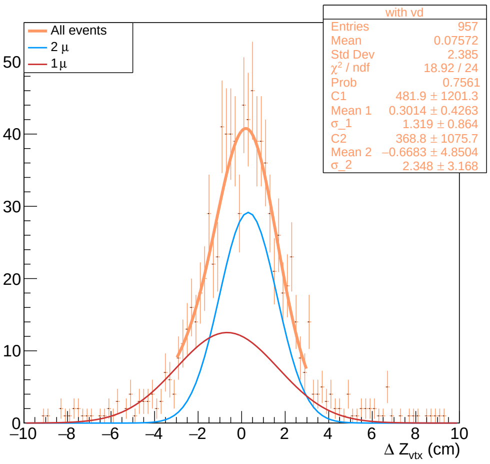

(c) C2 cell.

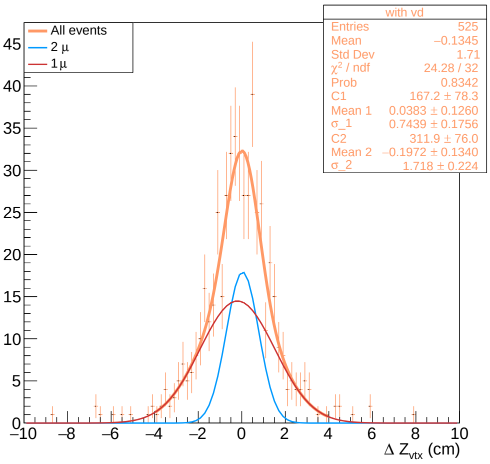

(d) C3 cell.

Figure A.5: Z_{vtx} resolution for the realistic hit treatment, considering the new FVTX detector layout.

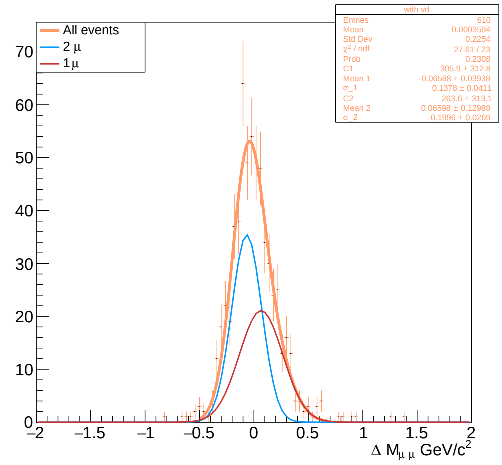

(a) W cell.

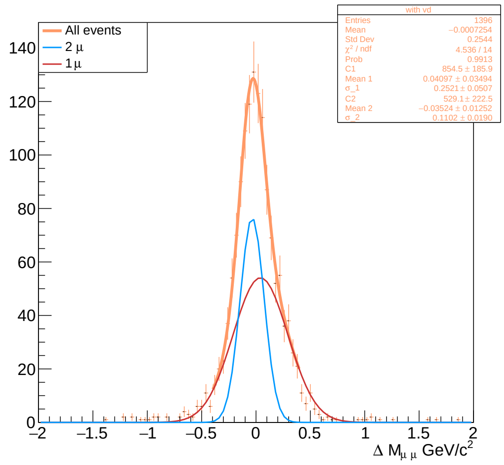

(b) C1 cell.

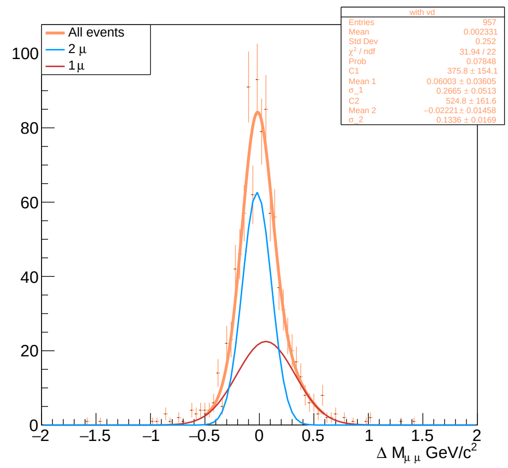

(c) C2 cell.

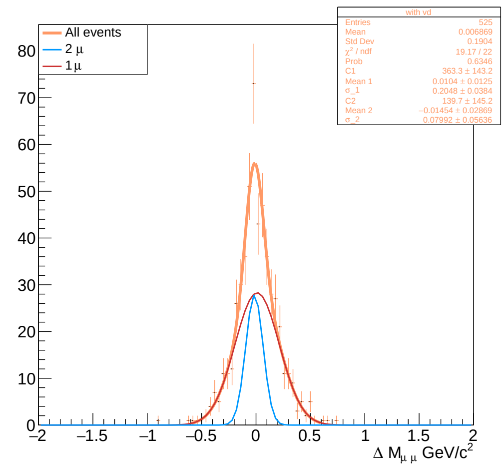

(d) C3 cell.

Figure A.6: Dimuon mass resolution for the realistic hit treatment, considering the new FVTX detector layout.